Banner appropriate to article type will appear here in typeset article

Velocity dip in turbulent mixed convection of an open Poiseuille–Rayleigh–Bénard channel

Ben-Rui Xu[1], Ao Xu[1,2] and Heng-Dong Xi[1,2]

[1]Institute of Extreme Mechanics, School of Aeronautics, Northwestern Polytechnical University, Xi'an 710072, PR China

[2]National Key Laboratory of Aircraft Configuration Design, Key Laboratory for Extreme Mechanics of Aircraft of Ministry of Industry and Information Technology, Xi'an 710072, PR China

Corresponding author: Ao Xu, axu@nwpu.edu.cn

We study the emergence of a velocity-dip phenomenon in turbulent mixed convection in open Poiseuille–Rayleigh–Bénard (PRB) channels with a free-slip upper boundary. Three-dimensional direct numerical simulations (DNS) are performed for Rayleigh numbers in the range $10^5 \leq Ra \leq 10^8$, at a fixed Prandtl number $Pr = 0.71$ and a bulk Reynolds number $Re_b = 2850$. In the shear-dominated regime, the flow is characterised by small-scale structures such as near-wall streaks. As buoyancy becomes comparable to shear, streamwise-oriented large-scale rolls emerge and span the full channel height. At higher Rayleigh numbers, buoyancy dominates and the rolls fragment, giving rise to a convection-cell-dominated regime. Short-time-averaged flow fields show that streamwise rolls transport low-speed fluid from the bottom wall towards the upper boundary, forming laterally extended low-speed regions, while roll fragmentation induces upstream low-speed regions near the upper boundary. Both mechanisms locally reduce the near-surface mean velocity, leading to a velocity dip in which the maximum mean streamwise velocity is located below the upper boundary. Consistent with the mean momentum budget, the near-surface region exhibits a large-scale Reynolds shear stress that exceeds the local total shear stress, implying a negative viscous contribution and a reversal of the mean velocity gradient. To model this behaviour, we propose a model based on a balance between buoyancy and shear production with dissipation, incorporating a linear wall-normal profile for the Reynolds shear stress, a wall-normal-independent buoyancy-production term, and a decomposition of the dissipation into shear-induced and buoyancy-induced contributions. Our model accurately reproduces the DNS mean velocity profiles across the explored Ra range.

Key words: Bénard convection, plumes/thermals, turbulent convection.

1. Introduction

Mixed convection, driven by the combined effects of shear and buoyancy forces, is ubiquitous in both natural and engineering systems (Caulfield 2021). For example, in the atmospheric boundary layer, the interaction between vertical buoyancy (induced by solar heating) and horizontal wind shear (induced by pressure gradients) can generate large-scale streamwise-oriented convective rolls (Stull 2012; Zhang 2024), commonly observed as cloud streets. In indoor ventilation scenarios, mixed convection caused by internal heat sources and mechanically driven airflow can produce a stratified temperature field, often characterised by an interface separating warm and cold regions (Yang *et al.* 2022). A canonical flow system for studying mixed convection is the Poiseuille–Rayleigh–Bénard (PRB) system, in which pressure-driven Poiseuille flow is superimposed on Rayleigh–Bénard (RB) convection (Pirozzoli *et al.* 2017; Blass *et al.* 2020, 2021; Xu *et al.* 2025). The control parameters of the PRB system include the Rayleigh number (Ra, defined below), which describes the relative strength of buoyancy compared with thermal and viscous diffusion (Verma 2018; Lohse & Shishkina 2024; Shishkina & Lohse 2024); the Prandtl number (Pr), which characterises the fluid's thermophysical properties; and the friction Reynolds number (Re_τ), which measures the intensity of near-wall shear. A key response parameter is the Nusselt number (Nu), which measures the global heat transfer efficiency.

Efforts have been devoted to understanding the dynamics of the PRB system (Pirozzoli *et al.* 2017; Blass *et al.* 2020, 2021; Xu *et al.* 2025). A distinguishing feature of such mixed convection is the formation of large-scale convective rolls that span the full channel height (Domaradzki & Metcalfe 1988; Pirozzoli *et al.* 2017), analogous to roll organisation in the atmospheric boundary layer (ABL) (Khanna & Brasseur 1998; Salesky *et al.* 2017). In the ABL, the balance between shear and buoyancy governs the local flow organisation. As stability decreases from near-neutral to strongly convective conditions, the flow transitions from near-wall low-speed streaks to large-scale horizontal rolls and, ultimately, to Rayleigh–Bénard-like cellular convection (Khanna & Brasseur 1998). This continuum was further quantified by Salesky *et al.* (2017) through the introduction of a "roll factor". Linear stability analyses in the turbulent regime have shown that the emergence of these rolls depends not only on the relative strengths of shear and buoyancy (Madhusudanan *et al.* 2022), but also on the Rayleigh number exceeding a critical threshold (Cossu 2022). Surface heterogeneity further modulates this process, as Schäfer *et al.* (2022) showed that spanwise-heterogeneous surfaces (streamwise-oriented ridges) delay the transition from forced convection to streamwise rolls and promote the fragmentation of streamwise convection. More recently, Feng *et al.* (2024) showed that temperature structures resemble streamwise-velocity structures mainly near the wall under neutral or stable stratification, whereas unstable stratification introduces buoyancy-driven large scales that dominate the outer layer and break this similarity.

In the PRB system, buoyancy–shear interaction alters both momentum and heat transport, leading to departures from canonical wall laws. On the momentum side, strong buoyancy forces induce a downward shift of the mean velocity profile, resulting in deviations from the classical logarithmic law. Scagliarini *et al.* (2015) attributed this shift to buoyancy-induced drag and proposed a modified logarithmic law that captures the interplay between buoyancy and shear. In terms of global heat-transfer efficiency, Pirozzoli *et al.* (2017) developed empirical correlations for Nu as a function of Ra and the bulk Reynolds number Re_b, extending earlier scaling arguments (Scagliarini *et al.* 2014; Pirozzoli *et al.* 2016). More recently, Xu *et al.* (2025) investigated the effect of temporally modulated thermal forcing on mixed convection, showing that low-frequency modulation can substantially

reorganise the flow and enhance heat transfer. Another canonical system for studying mixed convection is the Couette–Rayleigh–Bénard (CRB) system, in which shear is introduced by oppositely moving walls rather than by a pressure-driven flow; this system can be viewed as a counterpart to the PRB configuration (Yerragolam *et al.* 2024). Blass *et al.* (2020, 2021) extended the analysis to the CRB system and identified distinct *Nu* scaling regimes in the buoyancy- and shear-dominated limits. Yerragolam *et al.* (2024) further developed generalised scaling relations for both *Nu* and friction coefficients that are applicable to both PRB and CRB systems.

Most previous studies of mixed convection have focused on closed systems, in which both the upper and lower boundaries are no-slip walls. In contrast, many geophysical and environmental flows, such as those in the atmosphere, rivers, and oceans, are more accurately represented by open systems, for which the upper boundary can be modelled as a free-slip surface (Flores & Riley 2011). The absence of wall friction at the upper surface alters the flow structure and turbulence characteristics relative to closed configurations. For example, in open Poiseuille flow with a free-slip upper boundary, Yao *et al.* (2022) showed that the velocity profile deviates from that of closed-channel flows, particularly in the outer-layer region. They also reported a modification of the von Kármán constant, highlighting the distinct turbulence characteristics introduced by the free surface. Similarly, Pirozzoli (2023) observed an extended logarithmic region in the mean velocity profile, further confirming the influence of the free-slip surface on turbulent dynamics. In open RB convection with a free-slip upper boundary, the bulk temperature profile tends to shift towards the cooler boundary (Hay & Papalexandris 2019), and the overall heat transfer is enhanced compared with closed systems (Wang *et al.* 2020*b*). In open mixed convection systems, large-scale convective rolls can still form, but the resulting mean velocity profiles are generally more uniform in the wall-normal direction (Walker *et al.* 2014). Despite these advances, the physical mechanisms by which buoyancy modulates momentum and heat transfer in open mixed convection systems remain insufficiently understood.

In this study, we aim to reveal the mechanisms by which buoyancy modulates velocity profiles and heat transfer in open mixed convection systems. Motivated by the dynamics of mixed convection in the ABL and rivers, we consider an open PRB system with a free-slip and constant-temperature upper boundary (Atoufi *et al.* 2021) as an idealised configuration. Using DNS, we investigate the interplay between shear and buoyancy through detailed analyses of mean flow statistics and a triple decomposition of turbulent quantities. Based on these insights, we develop a velocity-dip model that accurately captures the velocity distribution in the outer layer of the open PRB system. The remainder of this paper is organised as follows. In § 2, we describe the numerical details of the DNS for the open PRB system. In § 3, we present a comprehensive analysis of the flow structures, velocity statistics, and heat-transfer characteristics. In § 4, the main findings of the present work are summarised.

2. Numerical methods

2.1. *Direct numerical simulation of mixed convection*

In incompressible mixed convection, both buoyancy and shear are incorporated into the momentum equation. Buoyancy is modelled using the Boussinesq approximation, in which temperature acts as an active scalar and drives motion in the wall-normal direction. The flow is also driven in the streamwise direction by a body force (equivalent to a mean pressure gradient) representing the imposed shear. The governing equations for momentum and temperature are

$$\nabla \cdot \boldsymbol{u} = 0, \tag{2.1}$$

$$\frac{\partial \boldsymbol{u}}{\partial t} + \boldsymbol{u} \cdot \nabla \boldsymbol{u} = -\frac{1}{\rho_0}\nabla P + \nu\nabla^2\boldsymbol{u} + f_b\,\hat{\boldsymbol{x}} + g\beta\,(T - T_0)\,\hat{\boldsymbol{y}}, \tag{2.2}$$

$$\frac{\partial T}{\partial t} + \boldsymbol{u} \cdot \nabla T = \alpha\nabla^2 T. \tag{2.3}$$

Here, $\boldsymbol{u}$ denotes the fluid velocity, while P and T denote the pressure and temperature, respectively. The constants β, ν and α are the thermal expansion coefficient, kinematic viscosity and thermal diffusivity, respectively. Reference-state quantities are indicated by the subscript zero, i.e. the reference density ρ_0 and reference temperature T_0. The body-force term f_b is adjusted to maintain a constant bulk flow rate and may vary weakly in time to keep the instantaneous bulk velocity fixed. The parameter g denotes the gravitational acceleration. The unit vectors $\hat{\boldsymbol{x}}$ and $\hat{\boldsymbol{y}}$ are aligned with the streamwise and wall-normal directions, respectively.

Using the non-dimensional variables

$$\boldsymbol{x}^* = \boldsymbol{x}/H, \quad t^* = t/(H/u_b), \quad \boldsymbol{u}^* = \boldsymbol{u}/u_b,$$
$$P^* = P/(\rho_0 u_b^2), \quad T^* = (T - T_0)/\varDelta_T, \quad f_b^* = f_b/(u_b^2/H), \tag{2.4}$$

where u_b is the bulk velocity, H is the channel height, and $\varDelta_T = T_{\text{hot}} - T_{\text{cold}}$ is the imposed temperature difference between the heated and cooled walls, equations (2.1)–(2.3) can be written in dimensionless form as

$$\nabla \cdot \boldsymbol{u}^* = 0, \tag{2.5}$$

$$\frac{\partial \boldsymbol{u}^*}{\partial t^*} + \boldsymbol{u}^* \cdot \nabla \boldsymbol{u}^* = -\nabla P^* + \frac{1}{Re_b}\nabla^2\boldsymbol{u}^* + f_b^*\hat{\boldsymbol{x}} + \frac{Ra}{Re_b^2 Pr}T^*\hat{\boldsymbol{y}}, \tag{2.6}$$

$$\frac{\partial T^*}{\partial t^*} + \boldsymbol{u}^* \cdot \nabla T^* = \frac{1}{Re_b Pr}\nabla^2 T^*. \tag{2.7}$$

The governing dimensionless parameters are the bulk Reynolds number Re_b, Rayleigh number Ra and Prandtl number Pr, defined as

$$Re_b = \frac{Hu_b}{\nu}, \qquad Ra = \frac{g\beta\varDelta_T H^3}{\nu\alpha}, \qquad Pr = \frac{\nu}{\alpha}. \tag{2.8}$$

We employ the spectral element method (Patera 1984), as implemented in the open-source Nek5000 solver (version v19.0), to perform the DNS. Nek5000 discretises the computational domain using high-order spectral elements, such that the effective grid resolution is given by the product of the number of spectral elements and the polynomial order; this is comparable to the total number of grid points used in traditional finite-difference or finite-volume methods. Following previous studies of turbulent thermal convection (Kooij *et al.* 2018), we adopt a polynomial order of $N = 8$ for both the velocity and pressure fields. Further details of the spectral element formulation and the Nek5000 solver can be found in Kooij *et al.* (2018). To ensure the accuracy and reliability of the DNS results, we additionally perform benchmark simulations of turbulent mixed convection and canonical open Poiseuille flow using Nek5000. As discussed in Appendix A, the present results show excellent agreement with the benchmark data of Pirozzoli *et al.* (2017);
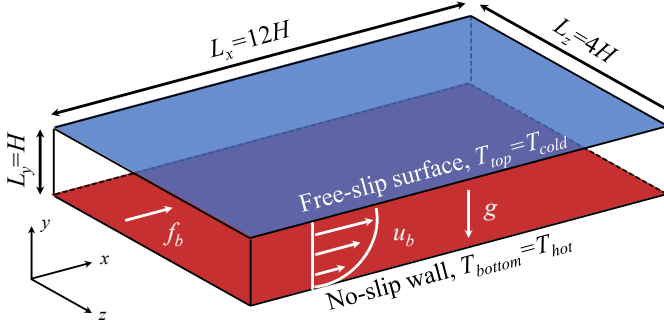
Focus on Fluids articles must not exceed this page length

Figure 1. Schematic of the open Poiseuille–Rayleigh–Bénard (PRB) channel. The bottom wall is no-slip and maintained at a constant hot temperature $T_{\text{bottom}} = T_{\text{hot}}$, while the top boundary is free-slip and held at a constant cold temperature $T_{\text{top}} = T_{\text{cold}}$.

Pirozzoli (2023); Yao *et al.* (2022), thereby confirming the accuracy and consistency of the numerical implementation.

2.2. *Simulation settings*

We explore the dynamics of mixed convection in a three-dimensional channel of dimensions $L_x \times L_y \times L_z = 12H \times H \times 4H$, as illustrated in figure 1. Here, x, y and z denote the streamwise, wall-normal and spanwise directions, respectively. The domain size is chosen to ensure adequate resolution of large-scale rolls in the spanwise direction, consistent with previous studies of mixed convection (Pirozzoli *et al.* 2017; Stevens *et al.* 2024). A detailed domain-size sensitivity analysis is provided in the Supplementary Materials. Periodic boundary conditions are applied in the streamwise and spanwise directions for both the velocity and temperature fields. In the wall-normal direction, a no-slip boundary condition is imposed at the bottom wall, while a free-slip boundary condition is applied at the top boundary, i.e. $\partial u/\partial y = \partial w/\partial y = v = 0$ at $y = H$ (Hay & Papalexandris 2019), corresponding to an infinite slip length (Xia 2024). This free-slip boundary is dynamically equivalent to a zero shear-stress condition and serves as an idealised model of a free surface without viscous resistance (Pirozzoli 2023). The grid is uniformly spaced in the streamwise and spanwise directions. In the wall-normal direction, an error-function mapping $\eta(\xi) = \text{erf}(a\xi/2)/\text{erf}(a/2)$, with $\xi \in [-1, 1]$ and $a = 3.2$, is used to cluster grid points near the walls (Pirozzoli *et al.* 2017, 2014). The clustering is symmetric about the channel mid-plane, allowing accurate resolution of both the near-wall viscous sublayer and the thermal boundary layers. For the thermal boundary conditions, the bottom wall is maintained at a constant hot temperature $T_{\text{bottom}} = T_{\text{hot}}$, while the top boundary is held at a constant cold temperature $T_{\text{top}} = T_{\text{cold}}$, yielding a fixed temperature difference $\Delta_T = T_{\text{bottom}} - T_{\text{top}}$. To trigger transition to turbulence, the initial velocity field is prescribed as a laminar Poiseuille flow superimposed with streak-like perturbations, following Schoppa & Hussain (2000). The initial temperature field is set uniformly to the mean temperature $(T_{\text{bottom}} + T_{\text{top}})/2$ throughout the domain.

In our simulations, the Rayleigh number is varied over the range $10^5 \leq Ra \leq 10^8$, while the Prandtl number is fixed at $Pr = 0.71$, corresponding to air. The bulk Reynolds number is maintained at $Re_b = 2850$, which yields a friction Reynolds number $Re_\tau \approx 180$ in the absence of buoyancy, i.e. for open Poiseuille flow. To characterise the relative influence of

Ra	Ri_b	Re_τ	Nu	ETT	$N_x \times N_y \times N_z$
1×10^5	1.7×10^{-2}	187.80	5.22	499.42	$200 \times 128 \times 104$
3×10^5	5.2×10^{-2}	194.94	6.29	301.40	$200 \times 128 \times 104$
1×10^6	1.7×10^{-1}	201.90	8.33	209.44	$200 \times 128 \times 104$
3×10^6	5.2×10^{-1}	232.72	11.59	175.36	$264 \times 160 \times 144$
1×10^7	1.7×10^0	276.65	17.37	126.55	$312 \times 192 \times 168$
3×10^7	5.2×10^0	319.64	25.71	43.39	$360 \times 232 \times 192$
1×10^8	1.7×10^1	379.09	39.66	34.39	$408 \times 256 \times 216$

Table 1. Flow parameters for DNS of the mixed convection in the open PRB channel. The columns from left to right indicating the following: Rayleigh number Ra, bulk Richardson number Ri_b, friction Reynolds number Re_τ at the bottom wall, Nusselt number Nu, time interval used for statistical averaging ETT (expressed in units of eddy turnover time H/u_τ), and grid number $N_x \times N_y \times N_z$.

shear and buoyancy, we use the bulk Richardson number $Ri_b = Ra/(Re_b^2 Pr)$, which spans the range $1.7 \times 10^{-2} \leq Ri_b \leq 1.7 \times 10^1$. The complete set of simulation parameters is summarised in table 1. For each case, we also report the corresponding friction Reynolds number Re_τ, Nusselt number Nu, and the time interval used for statistical averaging. The friction Reynolds number is defined as $Re_\tau = Hu_\tau/\nu$ (Yao *et al.* 2022; Pirozzoli 2023), where the friction velocity is $u_\tau = \sqrt{\tau_w/\rho_0}$ and $\tau_w = \rho_0 \nu \, \mathrm{d}\overline{u}/\mathrm{d}y$ denotes the wall shear stress at the bottom wall. The Nusselt number is evaluated as $Nu = \sqrt{RaPr/Ri_b} \langle v^* T^* \rangle_{V,t} + 1$, where $\langle \cdot \rangle_{V,t}$ denotes averaging over the computational volume and time.

To ensure adequate spatial and temporal resolution, we perform a detailed *a posteriori* verification based on several standard criteria: the grid spacing normalised by the viscous length scale $\delta_\nu = \nu/u_\tau$ (denoted by the superscript +), the number of grid points across the thermal boundary layer, and the maximum wall-normal grid spacing $(\Delta_g)_{max}$ and sampling time interval $(\Delta_t)_{max}$ relative to the Kolmogorov and Batchelor scales. In Nek5000, the computational domain is first partitioned into spectral elements, within which the solution is represented by Lagrange polynomials of order N at the Gauss–Lobatto–Legendre (GLL) collocation points. Accordingly, the grid numbers reported in table 1 correspond to the effective grid, i.e. the total number of GLL points in each direction. All resolution metrics are evaluated using the actual spacing between GLL points rather than the spectral-element size. Specifically, the wall-normal resolution, including $(\Delta y^+)_{min}$ and the Kolmogorov- and Batchelor-scale checks, is computed from the local spacing between adjacent GLL points. The streamwise and spanwise resolutions, Δx^+ and Δz^+, are evaluated using the mean spacing between GLL points, accounting for their non-uniform distribution within each element. The Kolmogorov length scale is estimated as $\eta_K = (\nu^3/\langle \varepsilon_u \rangle_{V,t})^{1/4}$, while the Batchelor length scale is $\eta_B = \eta_K Pr^{-1/2}$ (Silano *et al.* 2010). The Kolmogorov time scale is $\tau_\eta = \sqrt{\nu/\langle \varepsilon_u \rangle_{V,t}}$, where $\langle \varepsilon_u \rangle_{V,t}$ denotes the turbulent kinetic energy dissipation rate, computed as $\langle \varepsilon_u \rangle_{V,t} = \nu \langle (\partial_j u_i')^2 \rangle_{V,t}$, with u_i' being the velocity fluctuation. As summarised in table 2, the grid spacings in wall units satisfy

$$\Delta x^+ \leq 12, \qquad \Delta z^+ \leq 8, \qquad (\Delta y^+)_{min} \leq 0.11, \qquad (2.9)$$

which are sufficient to resolve near-wall structures in shear-dominated turbulence (Bernardini *et al.* 2014). Moreover, the resolution within the thermal boundary layers exceeds the criteria recommended by Shishkina *et al.* (2010) for purely thermal convection. In all cases, $(\Delta_g)_{max}$ remains below three times the Kolmogorov and Batchelor length scales,

Ra	$\varDelta x^+$	$(\varDelta y^+)_{\min}$	$\varDelta z^+$	N_{th}^{top}	N_{th}^{bottom}	$(\varDelta_g)_{\max}/\eta_K$	$(\varDelta_g)_{\max}/\eta_B$	$(\varDelta_t)_{\max}/\tau_\eta$
1×10^5	11.27	0.12	7.22	27	31	1.35	1.14	0.0069
3×10^5	11.70	0.12	7.50	22	29	1.39	1.17	0.0070
1×10^6	12.11	0.12	7.77	18	27	1.58	1.33	0.0073
3×10^6	10.58	0.11	6.46	19	28	1.61	1.36	0.0064
1×10^7	10.64	0.10	6.59	18	27	1.89	1.59	0.0054
3×10^7	10.64	0.09	6.65	18	24	2.22	1.87	0.0049
1×10^8	11.20	0.10	7.05	14	20	2.98	2.51	0.0045

Table 2. A *posteriori* verification of the spatial and temporal resolutions used in the simulations. The columns from left to right indicating the following: the Rayleigh number Ra; the grid spacing in wall units in the streamwise direction $\varDelta x^+$; the minimum wall-normal spacing $(\varDelta y^+)_{\min}$; the grid spacing in wall units in the spanwise direction $\varDelta z^+$; the number of grid points within the top thermal boundary layer N_{th}^{top}; the number of grid points within the bottom thermal boundary layer N_{th}^{bottom}; the maximum wall-normal grid spacing normalised by the Kolmogorov length $(\varDelta_g)_{\max}/\eta_K$; the maximum wall-normal grid spacing normalised by the Batchelor length $(\varDelta_g)_{\max}/\eta_B$; and the maximum sampling time interval normalised by the Kolmogorov time scale $(\varDelta_t)_{\max}/\tau_\eta$.

and $(\varDelta_t)_{\max}$ is substantially smaller than the Kolmogorov time scale. These checks confirm that the present simulations adequately resolve both shear- and buoyancy-driven turbulence. Statistical convergence is further verified by ensuring that the time histories of the root-mean-square velocity fluctuations $Re_{\text{r.m.s.}}$ (defined as $Re_{\text{r.m.s.}} = \sqrt{\langle|\boldsymbol{u}|^2\rangle_V}\, H/\nu$) and the Nusselt number Nu reach statistically steady states.

3. Results and discussion

3.1. *Flow organisation*

Figures 2 and 3 show instantaneous volume renderings of the temperature and streamwise-velocity fields over a range of Rayleigh numbers. At $Ra = 10^5$ (see figures 2a and 3a), the flow remains shear-dominated. The temperature and streamwise-velocity fields exhibit near-wall streaky structures, and no coherent large-scale roll organisation is observed, closely resembling the passive-scalar reference case (see figure 27 in Appendix B). For $Ra \geq 10^6$ (see figures 2b–d and 3b–d), coherent large-scale structures emerge and progressively reorganise the flow. Similar regime transitions have been reported in other mixed-convection systems. In closed configurations such as PRB and CRB, increasing buoyancy drives a transition from forced-convection streaks to streamwise-oriented large-scale rolls at moderate buoyancy and, in the strongly buoyant regime, to convection cells (Pirozzoli *et al.* 2017; Blass *et al.* 2020; Schäfer *et al.* 2022; Xu *et al.* 2024; Yerragolam *et al.* 2024). In the ABL, as stability decreases from neutral to convective conditions, the flow organisation evolves from near-surface low-speed streaks to large-scale horizontal rolls and ultimately to Rayleigh–Bénard-like convection cells (Khanna & Brasseur 1998; Weckwerth *et al.* 1999; Pino *et al.* 2003; Salesky *et al.* 2017; Salesky & Anderson 2018; Stoll *et al.* 2020).

To further extract the large-scale coherent structures in the open PRB system, we apply proper orthogonal decomposition (POD) to the velocity field. POD has been widely used to characterise large-scale circulation in convection (Castillo-Castellanos *et al.* 2019; Soucasse *et al.* 2019). Specifically, the spatio-temporal velocity field $\boldsymbol{u}(\boldsymbol{x}, t)$ is decomposed as
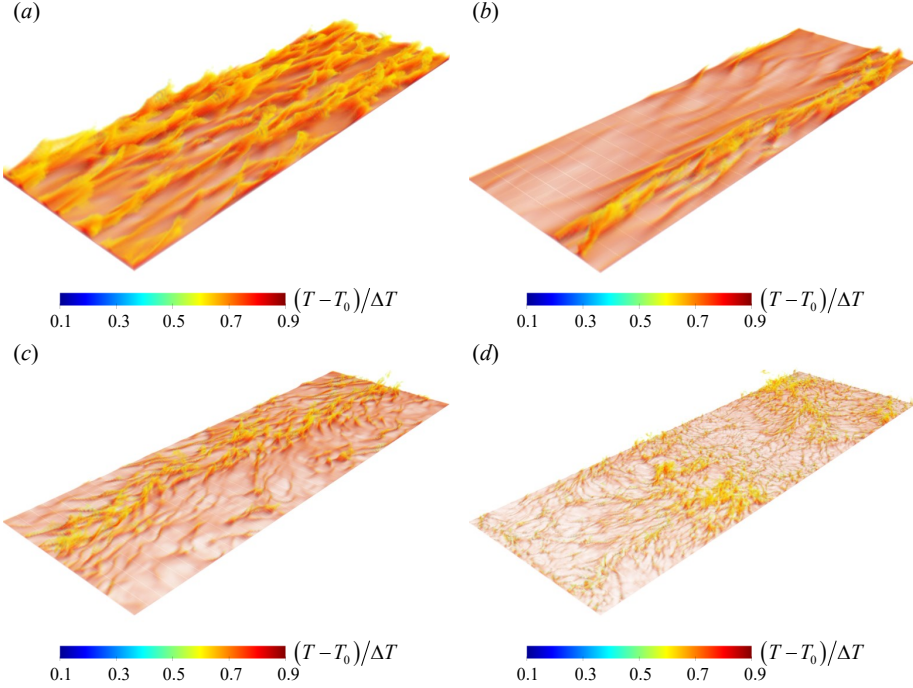
(*a*)

(*b*)

(*c*)

(*d*)

Figure 2. Instantaneous volume renderings of the temperature field at a fixed bulk Reynolds number $Re_b = 2850$. (*a*) $Ra = 10^5$, (*b*) $Ra = 10^6$, (*c*) $Ra = 10^7$ and (*d*) $Ra = 10^8$. The corresponding bulk Richardson numbers are 1.7×10^{-2}, 1.7×10^{-1}, 1.7×10^{0} and 1.7×10^{1}, respectively. Colour denotes the normalised temperature $(T - T_0)/\Delta_T$. Opacity increases monotonically with temperature to emphasise hot buoyant structures, while cooler regions are rendered transparent.

$$\boldsymbol{u}(\boldsymbol{x}, t) = \sum_{i=1}^{\infty} a_i(t)\,\boldsymbol{\varphi}_i(\boldsymbol{x}), \tag{3.1}$$

where $\boldsymbol{u} = [u(\boldsymbol{x}, t), v(\boldsymbol{x}, t), w(\boldsymbol{x}, t)]$, $\boldsymbol{\varphi}_i = [\varphi_i^u(\boldsymbol{x}), \varphi_i^v(\boldsymbol{x}), \varphi_i^w(\boldsymbol{x})]$ are the POD modes, and $a_i(t)$ are the corresponding temporal coefficients. The modal energy λ_i satisfies

$$\langle a_i(t) a_j(t) \rangle_t = \delta_{ij} \lambda_i, \tag{3.2}$$

where δ_{ij} is the Kronecker delta. Figures 4(*a*–*c*) show the most energetic POD mode computed over a window of $10 t_f$ from 200 snapshots, where $t_f = H/u_f$ and $u_f = \sqrt{g\beta\Delta TH}$. At $Ra = 10^6$ and 10^7 (see figures 4*a,b*), streamwise-oriented large-scale rolls span the full channel height, consistent with a mixed-convection regime in which shear and buoyancy are comparable. At $Ra = 10^8$ (see figure 4*c*), the roll organisation becomes fragmented, consistent with a transition towards convection cells. Figures 4(*d*–*f*) report the modal energy fractions $\lambda_i/\sum_i \lambda_i$. For $Ra \geq 10^6$, the leading mode alone accounts for more than 60% of the total energy, providing quantitative evidence that the dynamics are strongly dominated by a single large-scale coherent structure.

When convective rolls are present, shear and buoyancy are of comparable magnitude, so the bulk Richardson number is expected to be $Ri_b = O(1)$. In the present open PRB configuration, rolls are observed for $0.17 \leq Ri_b \leq 1.7$. In closed PRB channels, roll-

(*a*)

(*b*)

u / u_b

0.3 0.5 0.7 0.9 1.1 1.3

u / u_b

0.3 0.5 0.7 0.9 1.1 1.3

(*c*)

(*d*)

u / u_b

0.3 0.5 0.7 0.9 1.1 1.3
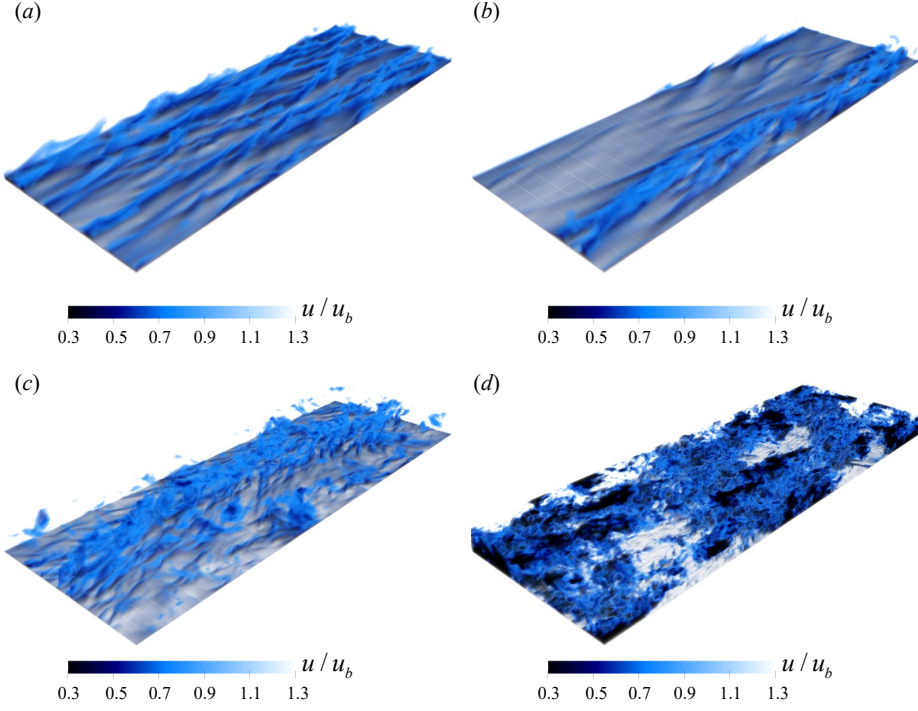
u / u_b

0.3 0.5 0.7 0.9 1.1 1.3

Figure 3. Instantaneous volume renderings of the streamwise velocity field at a fixed bulk Reynolds number $Re_b = 2850$. (*a*) $Ra = 10^5$, (*b*) $Ra = 10^6$, (*c*) $Ra = 10^7$ and (*d*) $Ra = 10^8$. The corresponding bulk Richardson numbers are 1.7×10^{-2}, 1.7×10^{-1}, 1.7×10^0 and 1.7×10^1, respectively. Colour denotes the normalised streamwise velocity u/u_b. Opacity decreases monotonically with streamwise velocity to emphasise low-speed structures, while higher-speed regions are rendered transparent.

(*a*)

(*b*)

(*c*)

(*d*)

(*e*)

(*f*)
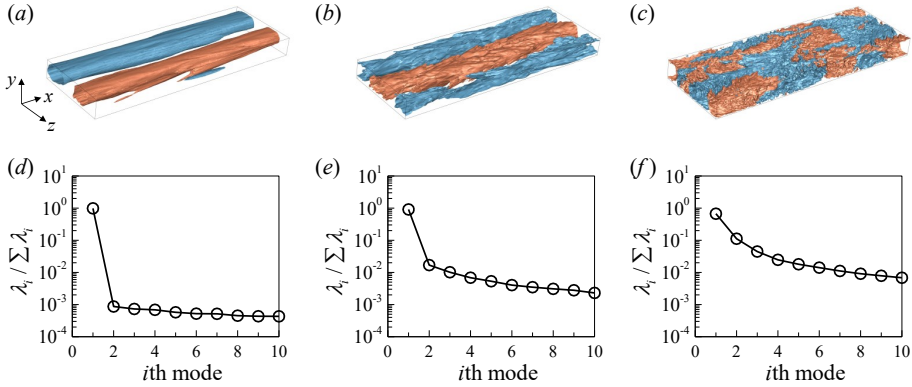
Figure 4. (*a–c*) The most energetic POD mode, shown as isosurfaces of the wall-normal velocity v (red denotes positive values and blue denotes negative values), and (*d–f*) the energy contained in each mode. Panels *(a,d)*, *(b,e)* and *(c,f)* correspond to $Ra = 10^6$, 10^7 and 10^8, respectively, at a fixed bulk Reynolds number $Re_b = 2850$. The corresponding bulk Richardson numbers are 1.7×10^{-1}, 1.7×10^0 and 1.7×10^1, respectively.
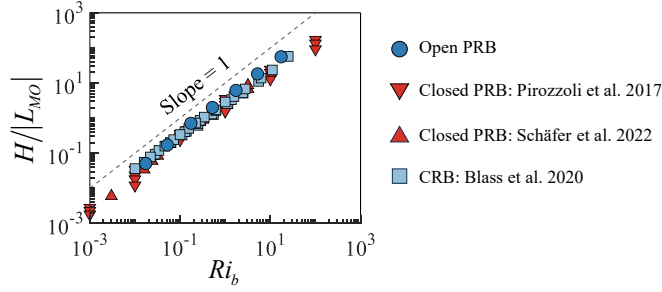
Figure 5. Non-dimensional Monin–Obukhov length $H/|L_{MO}|$ as a function of the bulk Richardson number Ri_b. Circles denote the present open PRB simulations, while triangles and squares correspond to closed PRB and CRB configurations taken from Pirozzoli *et al.* (2017), Schäfer *et al.* (2022) and Blass *et al.* (2020), respectively. The dashed line indicates a unit-slope power-law scaling, $H/|L_{MO}| \sim Ri_b$.

like large-scale organisation has been reported over a wider range, extending from $Ri_b = O(10^{-2})$ up to $Ri_b = O(10)$ (see figures 3 and 4 of Pirozzoli *et al.* (2017) and figures 6 and 7 of Schäfer *et al.* (2022)). To facilitate comparisons with atmospheric and wall-sheared convection studies, it is useful to express stability within the Monin–Obukhov framework. In the ABL, stability is commonly quantified by the non-dimensional Monin–Obukhov parameter, for example $z_i/|L_{MO}|$, where z_i denotes the boundary-layer height and $L_{MO} = -u_\tau^3/(\kappa \beta g \, \overline{v'T'})$ (Kader & Yaglom 1990). Large-scale convective rolls typically occur for $0.44 \leq z_i/|L_{MO}| \leq 8$ (Khanna & Brasseur 1998). The present open-channel configuration does not feature a dynamically evolving capping inversion or entrainment interface that would define a boundary-layer height z_i; we therefore adopt the outer stability measure $H/|L_{MO}|$. Care is required when comparing Monin–Obukhov lengths across studies because definitions can differ by constant factors and sign conventions. In particular, Pirozzoli *et al.* (2017) and Blass *et al.* (2020) employ a κ-free definition $\widetilde{L}_{MO} = u_\tau^3/(\beta g \, Q)$, where Q is the total vertical heat flux. For unstable stratification, this implies $|L_{MO}| = \widetilde{L}_{MO}/\kappa$. Under this mapping, the CRB condition reported by Blass *et al.* (2020), $\widetilde{L}_{MO} \gtrsim 0.5H$, corresponds to $H/|L_{MO}| \lesssim 0.8$ (for $\kappa = 0.4$). In our open PRB dataset, roll-containing cases correspond to $0.71 \lesssim H/|L_{MO}| \lesssim 6.16$. Moreover, our data indicate an approximately power-law relation $H/|L_{MO}| \sim Ri_b^{1.01}$ for open PRB. The corresponding trends inferred from Pirozzoli *et al.* (2017) (closed PRB) and Blass *et al.* (2020) (CRB) are $H/|L_{MO}| \sim Ri_b^{0.85}$ and $H/|L_{MO}| \sim Ri_b^{0.91}$, respectively. Figure 5 summarises these datasets. Despite quantitative differences between configurations, all cases exhibit the same qualitative behaviour. Increasing buoyancy relative to shear (larger Ri_b) is associated with increasing non-dimensional instability (larger $H/|L_{MO}|$ or $z_i/|L_{MO}|$).

To further examine the vertical organisation of turbulent structures, we consider instantaneous contours in horizontal x–z planes at three representative wall-normal locations: the near-wall region ($y^+ \approx 5$, figure 6), the mid-plane ($y/H = 0.5$, figure 7), and the near-surface region ($y/H \approx 0.98$, figure 8). In the near-wall plane at $y^+ \approx 5$, as shown in figure 6, the flow exhibits a strong negative correlation between u' and T' for $10^5 \leq Ra \leq 10^7$, consistent with ejection events in which low-speed, warm fluid is lifted away from the wall by streamwise vortices. These vortices generate elongated low-speed streaks (Cui *et al.* 2025) accompanied by high-temperature fluctuations. At $Ra = 10^5$, the streaks are relatively disordered and show limited spatial organisation, resembling passive-scalar transport in open Poiseuille flow (see figure 28 in Appendix B). As Ra increases to 10^6 and 10^7, the number of near-wall streaks increases and their spanwise modulation becomes
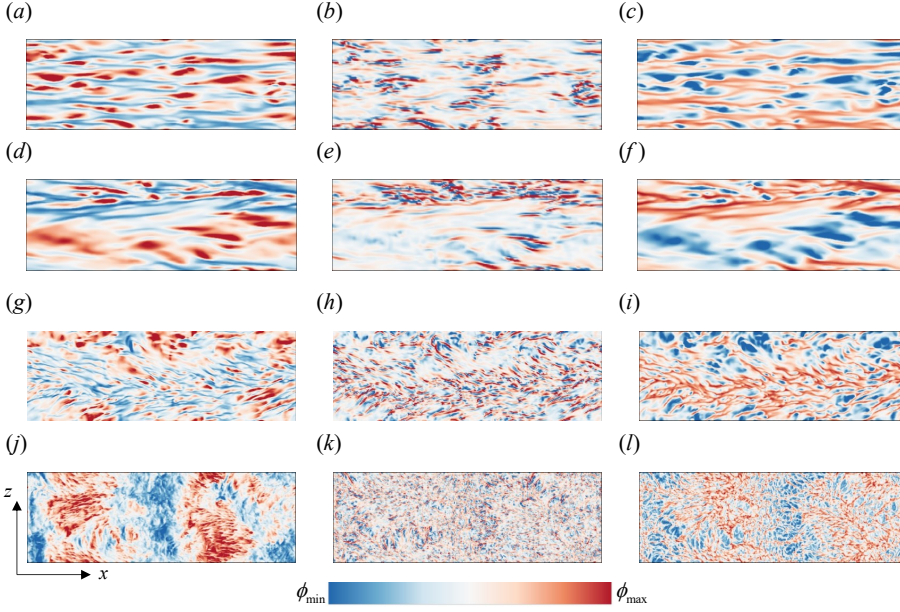
Figure 6. Instantaneous x–z plane contours in the near-wall region ($y^+ \approx 5$) at a fixed bulk Reynolds number $Re_b = 2850$. *(a,d,g,j)* streamwise-velocity fluctuation u', *(b,e,h,k)* wall-normal velocity fluctuation v' and *(c,f,i,l)* temperature fluctuation T' for *(a–c)* $Ra = 10^5$, *(d–f)* $Ra = 10^6$, *(g–i)* $Ra = 10^7$ and *(j–l)* $Ra = 10^8$. The corresponding bulk Richardson numbers are 1.7×10^{-2}, 1.7×10^{-1}, 1.7×10^0 and 1.7×10^1, respectively. The colour limits $\phi_{\min}$ and $\phi_{\max}$ correspond to $\pm 2\sigma_\phi$, where σ_ϕ is the standard deviation of the field shown in each panel (u', v' or T').

more pronounced. The streaks preferentially cluster beneath the ascending branches of the large-scale streamwise rolls, analogous to the modulation of near-wall structures by large-scale motions in high-Reynolds-number canonical channel flows (Toh & Itano 2005; Zhou *et al.* 2022, 2024). At $Ra = 10^8$, buoyancy dominates and the near-wall streamwise organisation becomes less coherent. The streamwise-velocity field develops alternating low- and high-speed bands along the streamwise direction (see figure 6*j–l*), while the streaks become shorter and less distinct. The temperature fluctuations concurrently exhibit a network-like pattern reminiscent of classical RB convection. The preferred orientation of these structures in the x and z directions is consistent with the rectangular domain geometry (Pirozzoli *et al.* 2017; Schäfer *et al.* 2022).

At the mid-plane of $y/H = 0.5$, as shown in figure 7, the wall-normal velocity fluctuations are stronger than near the wall and become positively correlated with temperature fluctuations, consistent with enhanced vertical convective heat transport. At $Ra = 10^5$, large-scale rolls are absent and the wall-normal velocity fluctuation v' exhibits little organised structure (see figure 7*b*). As Ra increases, streamwise-oriented rolls develop and organise the mid-plane flow over the full streamwise extent of the domain. Within the spanwise width ($L_z = 4H$), the flow is dominated by a single upwelling and a single downwelling region (see figures 7*e,h*), indicating a highly coherent large-scale circulation. The alternating low- and high-speed regions in the streamwise-velocity field (see figures 7*d,g*) align with the ascending and descending branches of this circulation, respectively. At $Ra = 10^8$, both the temperature and velocity fields become more fragmented, reflecting the breakdown of the previously coherent roll organisation under strong buoyancy forcing (Xu *et al.* 2025).
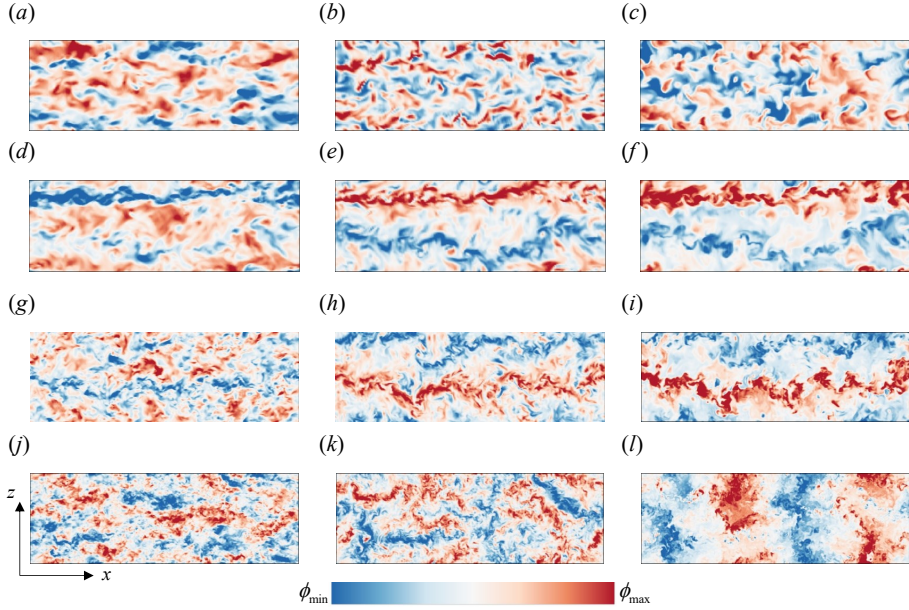
Figure 7. Instantaneous x–z plane contours in the mid-plane ($y/H = 0.5$) at a fixed bulk Reynolds number $Re_b = 2850$. *(a,d,g,j)* streamwise-velocity fluctuation u', *(b,e,h,k)* wall-normal velocity fluctuation v' and *(c,f,i,l)* temperature fluctuation T' for *(a–c) $Ra = 10^5$*, *(d–f) $Ra = 10^6$*, *(g–i) $Ra = 10^7$* and *(j–l) $Ra = 10^8$*. The corresponding bulk Richardson numbers are 1.7×10^{-2}, 1.7×10^{-1}, 1.7×10^{0} and 1.7×10^{1}, respectively. The colour limits $\phi_{\min}$ and $\phi_{\max}$ correspond to $\pm 2\sigma_\phi$, where σ_ϕ is the standard deviation of the field shown in each panel (u', v' or T').

In the near-surface region at $y/H \approx 0.98$, as shown in figure 8, the absence of wall shear suppresses the formation of near-wall-type streamwise vortices. Instead, the flow is characterised by small-scale upwelling and downwelling motions associated with surface-aligned and surface-attached vortices (Pinelli *et al.* 2022). Examining the wall-normal velocity fluctuations, we find that at low buoyancy, corresponding to the shear-dominated regime (see figure 8b), the surface-aligned vortices exhibit no clear preferential orientation. As buoyancy increases to $Ra = 10^6$ (see figure 8e), the vortical structures tend to align approximately perpendicular to the large-scale streamwise-oriented rolls and occur preferentially within the roll-descending regions. This behaviour is consistent with buoyancy-driven upwelling and downwelling superimposed on the background shear flow. With further increases in buoyancy (see figures 8h,k), the preferential alignment weakens and the vortices become more irregularly distributed, suggesting that the near-surface layer is populated by approximately isotropic small-scale motions rather than by an organised Rayleigh–Bénard-like cellular pattern. Consistent with the weak mean shear near the free-slip boundary, the temperature fluctuations in the near-surface region correlate more strongly with the wall-normal velocity fluctuations than with the streamwise-velocity fluctuations.

We further examine how streamwise-oriented rolls modulate near-wall streaks, in a manner analogous to the interaction between large-scale motions and near-wall structures in canonical shear flows (Toh & Itano 2005; Zhou *et al.* 2022, 2024). The roll-induced horizontal circulation generates a spanwise-varying advection field that clusters low-speed streaks within roll updrafts and depletes them in downdrafts, thereby promoting spanwise migration, merging and regeneration. Following Zhou *et al.* (2022), we track the spanwise
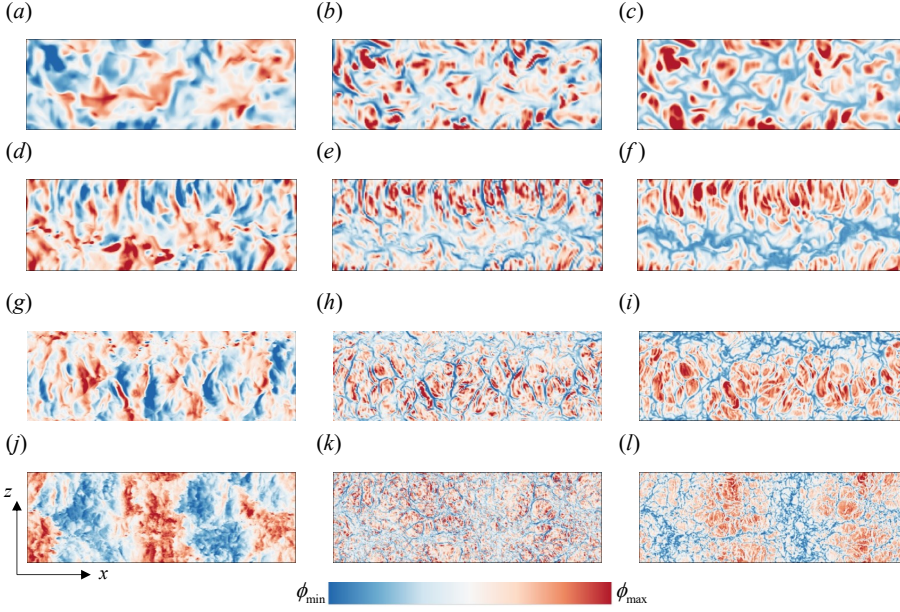
Figure 8. Instantaneous x–z plane contours in the near-surface region ($y/H \approx 0.98$) at a fixed bulk Reynolds number $Re_b = 2850$. (*a,d,g,j*) streamwise-velocity fluctuation u', (*b,e,h,k*) wall-normal velocity fluctuation v' and (*c,f,i,l*) temperature fluctuation T' for (*a–c*) $Ra = 10^5$, (*d–f*) $Ra = 10^6$, (*g–i*) $Ra = 10^7$ and (*j–l*) $Ra = 10^8$. The corresponding bulk Richardson numbers are 1.7×10^{-2}, 1.7×10^{-1}, 1.7×10^{0} and 1.7×10^{1}, respectively. The colour limits $\phi_{\min}$ and $\phi_{\max}$ correspond to $\pm 2\sigma_\phi$, where σ_ϕ is the standard deviation of the field shown in each panel (u', v' or T').

motion of low-speed streaks by identifying the spanwise locations of local minima of a streamwise-filtered streamwise-velocity fluctuation. Specifically, $z = z_m$ is defined as a local-minimum location of u'^{2D} if

$$u'^{2D}(t, x_r, y, z_m) < 0, \qquad \frac{\partial u'^{2D}}{\partial z}(t, x_r, y, z_m) = 0, \qquad \frac{\partial^2 u'^{2D}}{\partial z^2}(t, x_r, y, z_m) > 0. \quad (3.3)$$

Here u'^{2D} is obtained by filtering the original fluctuation u' along the streamwise direction,

$$u'^{2D}(t, x_r, y, z) = \frac{1}{\Delta x} \int_{x_r - \Delta x/2}^{x_r + \Delta x/2} u'(t, x, y, z) \, \mathrm{d}x, \qquad (3.4)$$

where x_r is the midpoint of the averaging interval and $\Delta x^+ = 400$ (Zhou *et al.* 2022). Figure 9 shows the temporal evolution of the identified local-minimum locations at different Ra. For $Ra = 10^5$, where large-scale streamwise rolls are essentially absent, the local-minimum locations are nearly uniformly distributed in the near-wall plane (see figure 9*a*), while in the mid-plane they exhibit a clustered distribution that preferentially resides in the low-speed region (see figure 9*b*). As Ra increases, the near-wall minima (see figures 9*c,e*) serve as a proxy for the instantaneous low-speed streak positions and organise into alternating clustered and sparse regions, consistent with roll updrafts and downdrafts, respectively. Moreover, minima in the sparse regions gradually drift towards the clustered regions, indicating a roll-induced spanwise migration. At mid-height (see figures 9*d,f*), the minima increasingly concentrate into an intensified low-speed band, consistent with
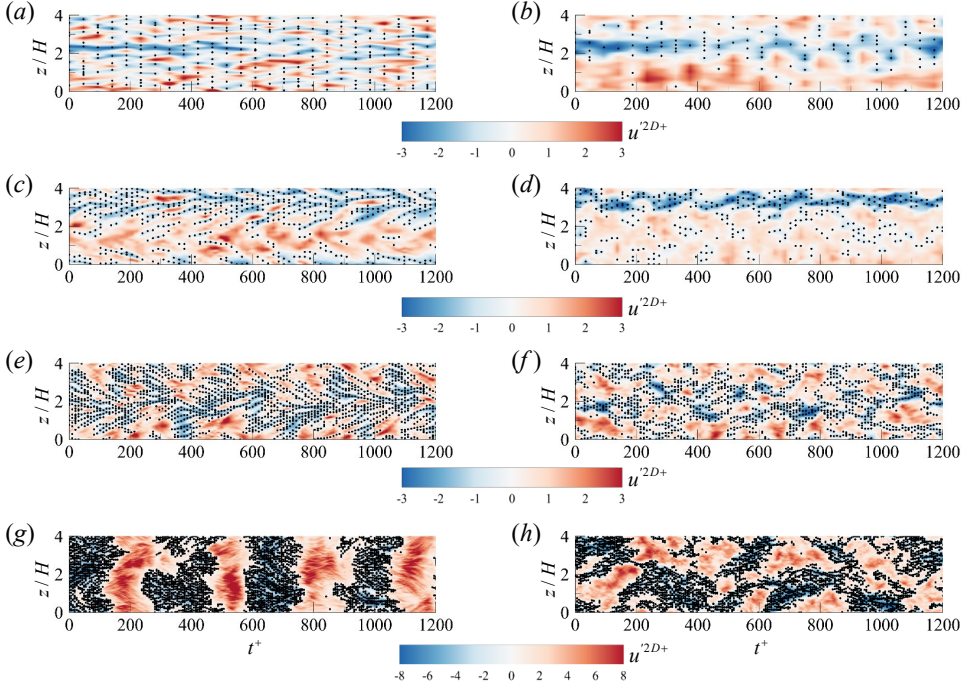
Figure 9. Temporal evolution of local-minimum positions (black dots) at *(a,c,e,g)* the near-wall region ($y^+ \approx 5$) and *(b,d,f,h)* the middle plane ($y/H = 0.5$) for *(a,b)* $Ra = 10^5$, *(c,d)* $Ra = 10^6$, *(e,f)* $Ra = 10^7$ and *(g,h)* $Ra = 10^8$, at a fixed bulk Reynolds number $Re_b = 2850$. The background colour contours show the streamwise-filtered streamwise-velocity fluctuation u'^{2D}.

upward transport and merging by the large-scale rolls, as also reported in ABL observations (Khanna & Brasseur 1998). The band is more fragmented at $Ra = 10^7$ than at $Ra = 10^6$. When the flow becomes convection-cell dominated at $Ra = 10^8$, the near-wall field exhibits an intermittent alternation between low- and high-speed regions over time (see figure 9*g*), reflecting strong modulation by the large-scale organisation superposed on the mean shear. In the mid-plane, the local-minimum locations appear more fragmented (see figure 9*h*) compared with $Ra = 10^7$.

To quantify how buoyancy modifies the flow organisation, we examine two-point correlations and premultiplied energy spectra of the wall-normal velocity fluctuations in the streamwise and spanwise directions, as shown in figures 10 and 11. For the two-point correlations (Pinelli *et al.* 2022), the streamwise correlation length in the bulk increases at $Ra = 10^6$ relative to $Ra = 10^5$ (see figures 10*a,c*), consistent with the emergence of coherent streamwise rolls. At $Ra = 10^7$ (see figure 10*e*), this coherence weakens and regions of negative correlation appear, suggesting the onset of roll fragmentation. At $Ra = 10^8$ (see figure 10*g*), the streamwise correlation alternates in sign, consistent with a more cellular organisation. The spanwise correlations show that at $Ra = 10^5$ (see figure 10*b*), a strong near-wall negative correlation reflects the updraft–downdraft pattern associated with near-wall streamwise vortices. As Ra increases (see figures 10*d,f*), a pronounced negative-correlation region develops in the bulk, implying an updraft–downdraft spacing of approximately $2H$, comparable to that reported for closed PRB (Pirozzoli *et al.* 2017). By contrast, CRB exhibits a shear-dependent spacing ranging from πH to $\pi H/2$ as the relative strengths of shear and buoyancy vary (Blass *et al.* 2020). At
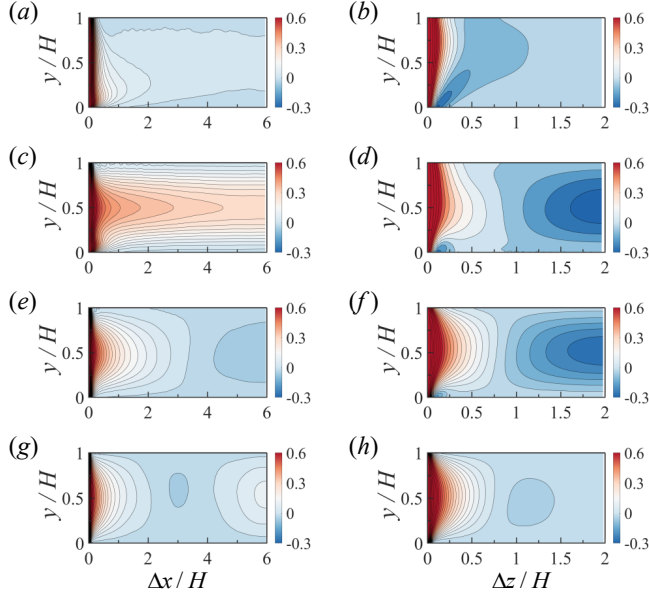
Figure 10. Two-point correlations of the wall-normal velocity fluctuation v' in the streamwise direction *(a,c,e,g)* and the spanwise direction *(b,d,f,h)* at *(a,b)* $Ra = 10^5$, *(c,d)* $Ra = 10^6$, *(e,f)* $Ra = 10^7$, and *(g,h)* $Ra = 10^8$, for a fixed bulk Reynolds number $Re_b = 2850$.

$Ra = 10^8$ (see figure 10h), the near-wall signature is markedly weakened, consistent with the disappearance of near-wall streamwise vortices and a transition towards a buoyancy-dominated cellular state.

The premultiplied spectra in figure 11 support the same interpretation. In the streamwise direction, at $Ra = 10^5$ (see figure 11a), the spectrum is dominated by a single peak at relatively short wavelengths, consistent with predominantly small-scale motions. At $Ra = 10^6$ (see figure 11c), no distinct outer-scale peak at finite λ_x is observed. This indicates that the roll signature in v' is not concentrated at a finite streamwise wavelength; instead, its distribution can be considered as streamwise unifrom (i.e. $k_x = 0$). Similar behaviour has been reported for roll-like large-scale motions in open-channel flows (Yao *et al.* 2022; Bauer *et al.* 2023). At $Ra = 10^7$ (see figure 11e), a pronounced peak emerges at $\lambda_x \approx 12H$, indicating the characteristic streamwise scale of the rolls. A secondary feature around $\lambda_x \approx 4H$ is also apparent, consistent with the onset of roll fragmentation. As the flow transitions towards a more cellular regime at $Ra = 10^8$ (see figure 11g), the dominant streamwise scale shifts to shorter wavelengths, with a peak near $\lambda_x \approx 6H$. In the spanwise direction, the dominant spectral signature shifts from near-wall vortical scales at $Ra = 10^5$ (see figure 11b) to an outer-scale, roll-related peak at $\lambda_z \approx 4H$ for $Ra = 10^6$ and 10^7 (see figures 11d,f). At $Ra = 10^8$ (see figure 11h), this peak moves to $\lambda_z \approx 2H$, consistent with a reduced lateral scale in the buoyancy-dominated regime.

Figures 12(a,b) show the mean streamwise-velocity profiles normalised by the bulk velocity u_b and the friction velocity u_τ, respectively. When scaled by u_b, the open PRB profiles lie above the open-Poiseuille profile for $y/H < 0.5$ and below it for $y/H > 0.5$ (see figure 12a), indicating a redistribution of mean momentum across the channel. For sufficiently strong buoyancy forcing (e.g. $Ra \geq 10^6$), the maximum mean velocity occurs below the free-slip boundary, yielding a velocity-dip profile (Ahamed & Kundu 2022; Chaudhry 2022). This contrasts with the canonical shear-driven open-channel case,
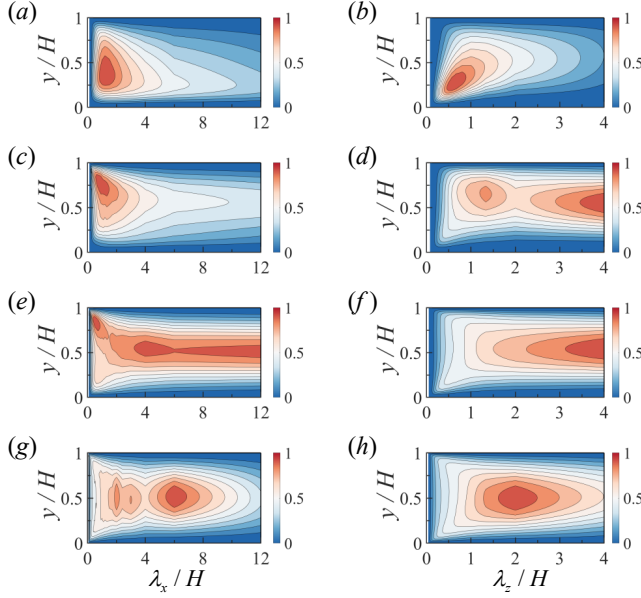
Figure 11. Premultiplied energy spectra of the wall-normal velocity fluctuation v' in the streamwise direction *(a,c,e,g)* and the spanwise direction *(b,d,f,h)* at *(a,b)* $Ra = 10^5$, *(c,d)* $Ra = 10^6$, *(e,f)* $Ra = 10^7$, and *(g,h)* $Ra = 10^8$, for a fixed bulk Reynolds number $Re_b = 2850$.

for which the mean velocity typically attains its maximum near the free surface under uniform forcing. When scaled by u_τ, the mean velocity in the outer layer of the open PRB system is systematically lower than that in open Poiseuille flow (see figure 12b). With increasing Ra, the entire outer-layer profile shifts downward, consistent with an increasing buoyancy-induced contribution to the overall resistance (Scagliarini *et al.* 2015). Similar downward shifts have been reported in closed PRB as the Richardson number increases (see figure 13(*b*) of Pirozzoli *et al.* (2017)); however, a velocity dip is not observed in that configuration. Velocity-dip profiles have also been documented in narrow open-channel flows, where sidewall-induced secondary motions reduce the centreline velocity (Yang *et al.* 2004, 2006). In that setting, Reynolds-stress redistribution plays a central role in shaping the mean profile. An atmospheric analogue is provided by low-level jets (LLJs), which exhibit a nose-shaped wind profile and may arise from several mechanisms, including inertial oscillations, baroclinicity and terrain effects (Stensrud 1996). LLJs are frequently associated with severe convective events because they enhance the transport of heat and moisture and can promote convective organisation (Luiz & Fiedler 2024; Saulo *et al.* 2007). While the physical setting differs, these examples highlight that interactions between shear, buoyancy and large-scale organisation can produce nose-shaped mean-velocity profiles, consistent with the behaviour observed here.

Turning to the mean temperature profile (see figure 12c), at $Ra = 10^5$ the flow remains in a shear-dominated regime and coherent roll structures are absent. Vertical mixing is then relatively weak, and the mean temperature decreases monotonically from the heated bottom wall towards the upper boundary. For $10^6 \le Ra \le 10^8$, enhanced vertical transport associated with large-scale motions yields a comparatively uniform bulk temperature together with steeper near-boundary gradients, consistent with thinner thermal boundary layers. In addition, the bulk mean temperature in the present open configuration is lower than that reported for mixed convection with symmetric no-slip upper and lower boundaries. As
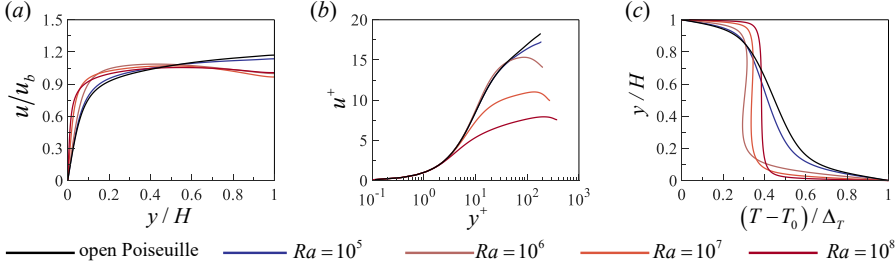
Figure 12. Mean wall-normal profiles at $Re_b = 2850$. (*a*) Mean streamwise velocity normalised by the bulk velocity u_b. (*b*) Mean streamwise velocity normalised by the friction velocity u_τ. (*c*) Mean temperature normalised by the imposed temperature difference Δ_T. The black lines correspond to open Poiseuille flow with buoyancy absent (passive-scalar temperature).

Ra increases, the bulk temperature shifts towards $T_{\text{mean}} = 0.5$, i.e. the arithmetic mean of the two wall temperatures, in agreement with previous studies of open convection systems (Hay & Papalexandris 2019, 2020). This trend is consistent with an upward displacement of the upper thermal boundary layer under the free-slip condition, which removes tangential shear at the upper boundary (Huang *et al.* 2022).

3.2. *Statistics of large-scale rolls*

The onset of the velocity dip coincides with the formation of large-scale rolls, which motivates an examination of how roll dynamics relate to the reduction of near-surface streamwise velocity. To this end, we analyse how the large-scale organisation modulates the spatial distribution of streamwise momentum. To isolate the large-scale contribution, we apply short-time averaging over a window of $10t_f$, where $t_f = H/u_f$. Figures 13(*a–c*) show the resulting velocity fields in the y–z plane at $Ra = 10^6$, for which the dominant coherent structures are streamwise-oriented rolls. Near the bottom wall, dispersed low-speed streaks progressively merge into coherent low-speed regions (see figure 9), which are then advected upward within buoyancy-driven updrafts. Upon approaching the free-slip boundary, these low-speed regions spread laterally in the spanwise direction, producing localised reductions of the near-surface streamwise velocity. This roll-mediated pathway is absent in the open-Poiseuille reference case (see figure 13*d*), where the lack of large-scale rolls precludes sustained upward transport and near-surface lateral spreading of low-speed fluid.

At $Ra = 10^8$, the streamwise-oriented large-scale rolls become fragmented and the flow transitions towards a cellular organisation with a more complex large-scale structure. We therefore examine short-time-averaged flow fields at $Ra = 10^8$ in the y–z plane (see figures 14*a,b*) and in the x–y plane (see figures 14*c,d*). The fragmented roll organisation induces large-scale circulations in both planes and is accompanied by a non-uniform distribution of the streamwise velocity. Upstream of these circulations (e.g. at $x/H = 3$ in figure 14*d*), low-speed zones form near the free-slip boundary, and the corresponding streamwise-velocity profile exhibits a clear dip. By contrast, at downstream locations (e.g. $x/H = 6$ in figure 14*d*), the streamwise velocity increases monotonically towards the free-slip boundary. Such spatial variability is absent in the open-Poiseuille reference case (see figure 14*e*). These observations indicate that, in the buoyancy-dominated regime, large-scale circulations create intermittent near-surface low-speed zones which, upon averaging, are consistent with the emergence of a mean velocity-dip profile. Overall, strong buoyancy modulates the streamwise velocity through the associated large-scale organisation and promotes near-surface low-speed regions.
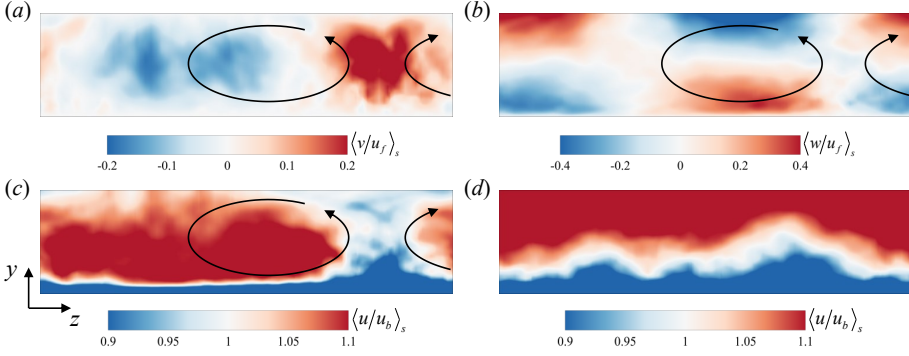
Figure 13. Short-time-averaged fields in the y–z plane at $x = 0$. (a) $\langle v/u_f \rangle_s$. (b) $\langle w/u_f \rangle_s$. (c) $\langle u/u_b \rangle_s$ for the open PRB case at $Ra = 10^6$ and $Re_b = 2850$. (d) $\langle u/u_b \rangle_s$ for the open Poiseuille reference case at $Re_b = 2850$. Arrows indicate the direction of the large-scale roll circulation.
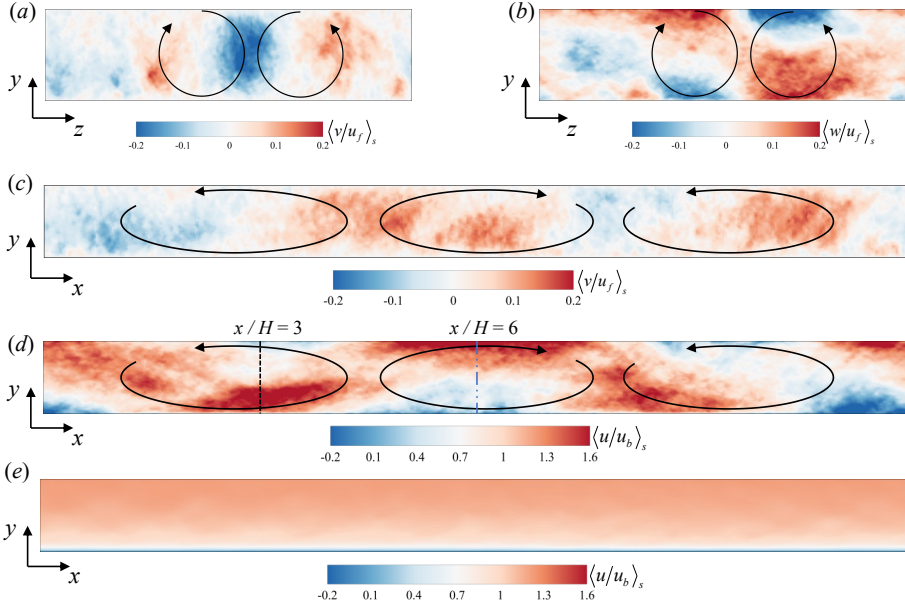

Figure 14. Short-time-averaged flow fields at $Ra = 10^8$ and $Re_b = 2850$. (a,b) Fields in the y–z plane at $x = 0$: (a) wall-normal velocity $\langle v/u_f \rangle_s$ and (b) spanwise velocity $\langle w/u_f \rangle_s$. (c,d) Fields in the x–y plane at $z = 0$: (c) wall-normal velocity $\langle v/u_f \rangle_s$ and (d) streamwise velocity $\langle u/u_b \rangle_s$. Arrows indicate the direction of the large-scale circulation, and dashed vertical lines mark the streamwise locations $x/H = 3$ and $x/H = 6$. (e) Streamwise velocity $\langle u/u_b \rangle_s$ for the open Poiseuille reference case at $Re_b = 2850$.

The large-scale organisation is not stationary in the horizontal plane. We therefore examine the temporal evolution of the streamwise-oriented rolls and the cellular pattern, as shown in figure 15. At $Ra = 10^6$, the streamwise rolls persist over the analysed interval, but their spanwise position drifts in time rather than remaining locked to a fixed lateral location (see figure 15a). Although such drift resembles the slow meandering reported in RB convection, in the present configuration it is more consistent with advection and reorganisation under the imposed mean shear than with shear-free reorientation of a domain-filling large-scale circulation (LSC) (Niemela *et al.* 2001; Brown *et al.* 2005; Xi &

Xia 2008). At $Ra = 10^8$, the flow is better characterised as a roll-fragmentation or cellular regime than as a single coherent domain-filling LSC. Over a representative interval of approximately $40t_f$, hot and cold regions alternate and migrate in time (see figures 15d,e). The wall-normal velocity field exhibits a more intricate evolution (see figures 15b,c), yet recurrent upwelling and downwelling signatures remain evident at multiple locations. The observed migration of the cellular pattern is consistent with modulation by the mean streamwise shear. Overall, we find no evidence for intermittent large-amplitude directional reorientation of a single coherent LSC analogous to classical RB convection. Instead, at $Ra = 10^8$ the large-scale organisation remains statistically robust in its dominant structures and length scales, while exhibiting temporal variability and lateral drift associated with a fragmented shear-influenced cellular regime.
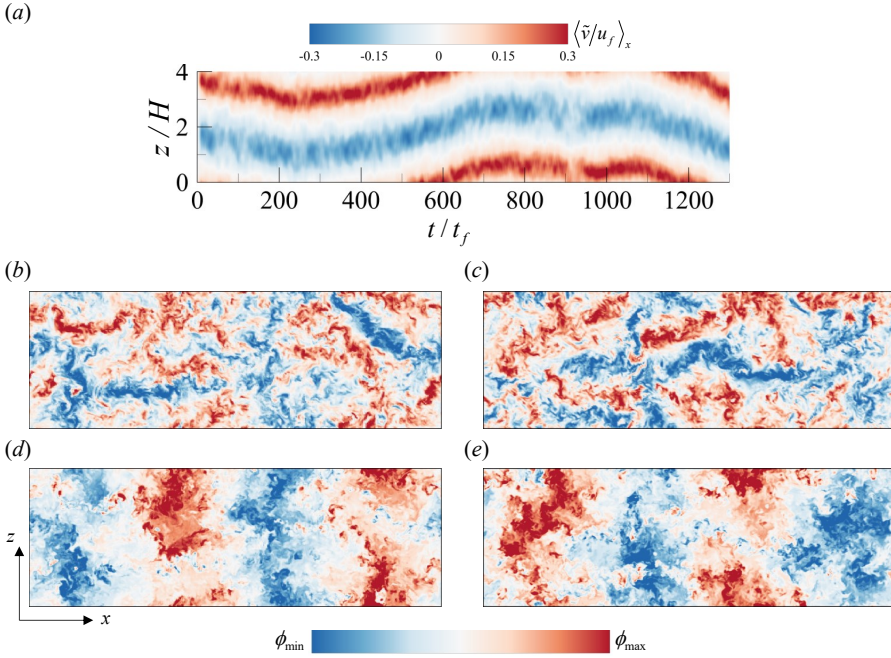

Figure 15. (*a*) Time evolution of the streamwise-averaged large-scale wall-normal velocity fluctuation $\langle \tilde{v}/u_f \rangle_x$ at $y/H = 0.5$. Instantaneous contours at $y/H = 0.5$ of (*b,c*) v'/u_τ and (*d,e*) T'/Δ_T at times t_0 (*b,d*) and $t_0 + 40t_f$ (*c,e*).

To quantify the dynamics of the large-scale organisation, we adopt a triple decomposition of an instantaneous flow quantity $\phi(x, y, z, t)$,

$$\phi(x, y, z, t) = \overline{\phi}(y) + \tilde{\phi}(x, y, z, t) + \phi''(x, y, z, t), \qquad (3.5)$$

where $\overline{\phi}(y)$ is the mean component obtained by horizontal (x–z) and long-time averaging and therefore depends only on y, $\tilde{\phi}(x, y, z, t)$ is the large-scale component associated with the slowly varying roll or cellular organisation, and $\phi''(x, y, z, t)$ denotes the residual small-scale fluctuations. We define the short-time-averaged field as

$$\langle \phi \rangle_s (x, y, z, t) = \overline{\phi}(y) + \tilde{\phi}(x, y, z, t), \qquad (3.6)$$

so that

B.-R. Xu, A. Xu and H.-D. Xi

$$\tilde{\phi} = \langle \phi \rangle_s - \overline{\phi}, \qquad \phi'' = \phi - \langle \phi \rangle_s. \tag{3.7}$$

The short-time average is introduced to separate the slowly varying large-scale contribution $\tilde{\phi}$ from the faster smaller-scale residual ϕ''. In this framework, $\overline{\phi}(y)$ represents the background profile obtained from long spatio-temporal averaging, whereas $\tilde{\phi}$ captures coherent organisation within a finite averaging window. Similar decompositions have been employed in previous studies of mixed convection and wall-bounded turbulence (Schäfer *et al.* 2022). The dependence of $\overline{\phi}$ on y alone follows from the assumption of a parallel mean flow and statistical homogeneity in the horizontal directions at a fixed wall-normal height. Following Cossu *et al.* (2009); Cossu (2022), we treat the mean statistics as homogeneous in x and z at a given y (Reynolds & Hussain 1972), an assumption supported by the horizontal drift of the large-scale organisation (see figure 15). Under this assumption, the mean velocity field is $\overline{\boldsymbol{u}} = [\overline{u}(y), 0, 0]$, and mean quantities can be computed via horizontal and temporal averaging, as standard in canonical channel flows (Lee & Lee 2015), mixed-convection channel flows (Scagliarini *et al.* 2015; Cossu 2022), and other turbulent flows (Galanti & Tsinober 2004; Djenidi *et al.* 2013).

Applying the triple decomposition to the streamwise momentum equation and subsequently performing long-time and horizontal averaging, we obtain the mean streamwise momentum equation

$$\frac{\partial \overline{u}}{\partial t} + \overline{u}\frac{\partial \overline{u}}{\partial x} + \overline{v}\frac{\partial \overline{u}}{\partial y} + \overline{w}\frac{\partial \overline{u}}{\partial z} = -\frac{1}{\rho_0}\frac{\partial \overline{p}}{\partial x} + \nu\left(\frac{\partial^2 \overline{u}}{\partial x^2} + \frac{\partial^2 \overline{u}}{\partial y^2} + \frac{\partial^2 \overline{u}}{\partial z^2}\right) - \left(\frac{\partial \overline{\tilde{u}\tilde{u}}}{\partial x} + \frac{\partial \overline{\tilde{u}\tilde{v}}}{\partial y} + \frac{\partial \overline{\tilde{u}\tilde{w}}}{\partial z}\right)$$
$$- \left(\frac{\partial \overline{u''u''}}{\partial x} + \frac{\partial \overline{u''v''}}{\partial y} + \frac{\partial \overline{u''w''}}{\partial z}\right) + f_b. \tag{3.8}$$

Assuming statistical stationarity and a parallel mean flow that is homogeneous in the horizontal directions (x, z) at each fixed wall-normal location y, the mean momentum balance simplifies to a one-dimensional form (this reduction is also confirmed from the DNS, not shown for brevity),

$$\frac{1}{\rho_0}\frac{\mathrm{d}\tau_t}{\mathrm{d}y} + f_b = 0. \tag{3.9}$$

Here, the total shear stress is defined as

$$\tau_t(y) = \rho_0\left(\nu\frac{\mathrm{d}\overline{u}}{\mathrm{d}y} - \overline{\tilde{u}\tilde{v}} - \overline{u''v''}\right), \tag{3.10}$$

where $\rho_0 \nu\, \mathrm{d}\overline{u}/\mathrm{d}y$ denotes the viscous shear stress, $-\rho_0\overline{\tilde{u}\tilde{v}}$ the large-scale contribution to the Reynolds shear stress, and $-\rho_0\overline{u''v''}$ the small-scale contribution. Accordingly, the total Reynolds shear stress satisfies

$$-\rho_0\overline{u'v'} = -\rho_0\overline{\tilde{u}\tilde{v}} - \rho_0\overline{u''v''}. \tag{3.11}$$

Figure 16 shows wall-normal profiles of the stress components normalised by the wall shear stress τ_w for both open Poiseuille flow and open PRB flow. In open Poiseuille flow (see figure 16a), the small-scale Reynolds shear stress $-\rho_0\overline{u''v''}$ dominates the outer layer.
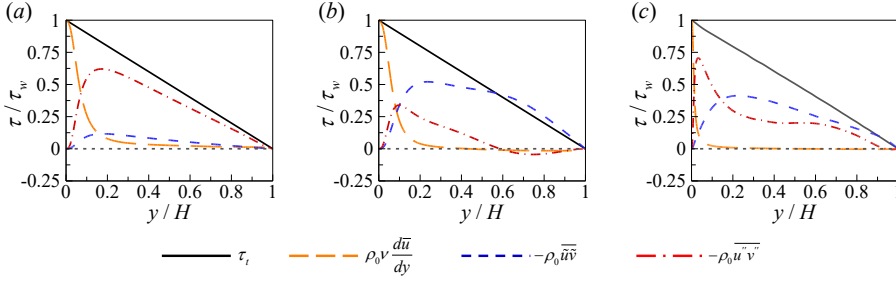
0 X0-20

Figure 16. Wall-normal profiles of shear-stress components in the streamwise momentum balance for open Poiseuille flow at (*a*) $Re_b = 2850$ and open PRB flow at (*b*) $Ra = 10^6$ and (*c*) $Ra = 10^8$, both with $Re_b = 2850$. The grey dashed line indicates $\tau/\tau_w = 0$.
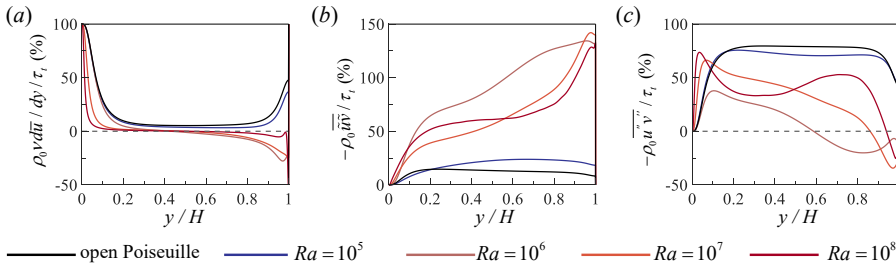

Figure 17. Wall-normal profiles of (*a*) the viscous shear stress $\rho_0 \nu \, d\overline{u}/dy$, (*b*) the large-scale Reynolds shear stress $-\rho_0 \overline{\tilde{u}\tilde{v}}$, and (*c*) the small-scale Reynolds shear stress $-\rho_0 \overline{u''v''}$ at $Re_b = 2850$ (open Poiseuille and open PRB cases as indicated in the legend). All stresses are shown as percentages of the local total shear stress, i.e. $100 \times (\cdot)/\tau_t(y)$. The grey dashed lines in (*a*) and (*c*) denote zero.

By contrast, in open PRB (see figures 16*b*,*c*), the large-scale contribution $-\rho_0 \overline{\tilde{u}\tilde{v}}$ becomes dominant in the outer region, effectively replacing the small-scale contribution there.

 To quantify how the large-scale roll organisation redistributes shear stress, we examine wall-normal profiles of the viscous shear stress and the large- and small-scale contributions to the Reynolds shear stress, each normalised by the local total shear stress $\tau_t(y)$, as shown in figure 17. When large-scale rolls are present ($Ra \geq 10^6$), the viscous contribution becomes strongly negative in the near-surface region (see figure 17*a*), consistent with a local reversal of the mean shear associated with the velocity-dip profile. By contrast, in cases without roll organisation ($Ra < 10^6$ and open Poiseuille flow), the viscous contribution remains positive throughout the domain. Concurrently, the relative contribution of the large-scale Reynolds shear stress increases significantly in roll-containing cases and can locally exceed unity near the free-slip boundary (see figure 17*b*). Such an "overshoot" indicates that the remaining stress contributions must locally compensate with the opposite sign, consistent with the simultaneous appearance of negative viscous stress and a reduced small-scale Reynolds stress (see figure 17*c*). Overall, these trends indicate that the velocity dip is accompanied by a roll-driven redistribution of stress among viscous, large-scale, and small-scale components in the near-surface region.

 Large-scale rolls also exert a strong influence on heat transfer and on the friction coefficient. Regarding heat transfer, the triple decomposition enables the Nusselt number to be separated into large-scale and small-scale convective contributions,
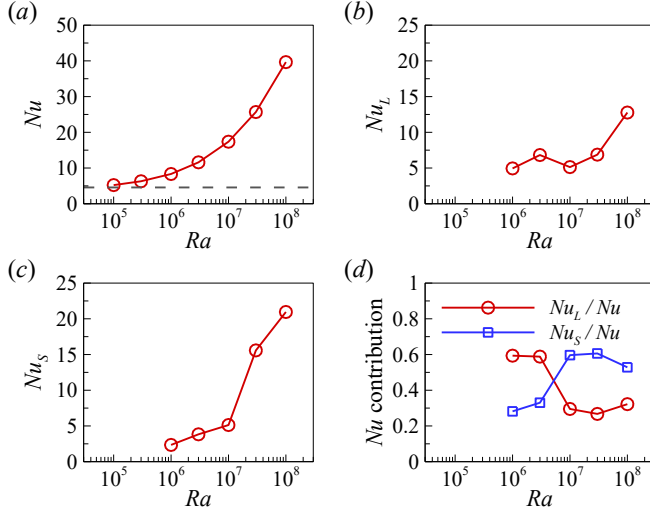
Figure 18. Nusselt number as a function of the Rayleigh number Ra in the open PRB system. (*a*) Total Nusselt number Nu, (*b*) large-scale contribution Nu_L, (*c*) small-scale contribution Nu_S, and (*d*) relative contributions of the large- and small-scale components to Nu. The grey dashed line in (*a*) denotes the Nusselt number for open Poiseuille flow with temperature treated as a passive scalar at $Ra = 0$ and $Re_b = 2850$.

$$
\begin{aligned}
Nu &= \sqrt{RaPr/Ri_b}\, \langle v^*T^* \rangle_{V,t} - \langle \partial T^*/\partial y^* \rangle_{V,t} \\
&= \sqrt{RaPr/Ri_b}\left(\langle \tilde{v}^*\tilde{T}^* \rangle_{V,t} + \langle v''^*T''^* \rangle_{V,t} \right) + 1 \\
&= Nu_L + Nu_S + 1,
\end{aligned}
\tag{3.12}
$$

where Nu_L and Nu_S denote the large-scale and small-scale convective contributions, respectively. Their dependence on Ra is shown in figure 18. As shown in figure 18(*a*), the total heat-transfer efficiency increases monotonically with Ra. However, because shear and buoyancy compete, a simple power-law Nu–Ra scaling of the type proposed for shear-free convection does not emerge in the present mixed-convection regime (Stevens *et al.* 2013; Wang *et al.* 2020*a*). Figure 18(*b*) shows that, within the roll-dominated regime ($10^6 \leq Ra \leq 10^7$), the increase of Nu_L is comparatively modest. By contrast, Nu_L rises sharply at $Ra = 10^8$, where the streamwise rolls fragment and the flow transitions towards a more cellular organisation. This enhancement is consistent with the emergence of stronger vertical motions that provide efficient pathways for convective transport (Xu *et al.* 2023). Compared with coherent streamwise-oriented rolls, the fragmented organisation yields a larger number of vertical transport channels (see figure 14*a*), thereby increasing Nu_L. On the other hand, figure 18(*c*) shows that the overall growth of Nu with Ra is primarily driven by the small-scale contribution Nu_S. This is particularly evident at $Ra = 3 \times 10^7$, where Nu_L varies only weakly while Nu_S increases substantially. Figure 18(*d*) summarises the relative contributions of the large- and small-scale components. For $Ra \geq 10^7$, heat transfer is dominated by small-scale structures, whereas for $Ra \leq 3 \times 10^6$ the large-scale rolls account for the larger fraction. The crossover occurs in the range $3 \times 10^6 < Ra < 10^7$. Note that at $Ra = 10^5$ the temperature field behaves similarly to a passive scalar because coherent large-scale rolls are absent; consequently, this case is omitted from figures 18(*b–d*).

For the friction coefficient C_f, which is defined as $C_f = 2\tau_w/(\rho_0 u_b^2)$, we employ the Fukagata–Iwamoto–Kasagi (FIK) identity (Fukagata *et al.* 2002) to decompose C_f into a laminar contribution and a turbulent contribution, and apply the triple decomposition (i.e. the turbulent contribution is further separated into large- and small-scale parts),

$$
\begin{aligned}
C_f &= \frac{6}{Re_b} + \frac{6}{u_b^2} \int_0^1 (1-\eta)\left(-\overline{u'v'}\right) \mathrm{d}\eta \\
&= \underbrace{\frac{6}{Re_b}}_{C_{f,L}} + \underbrace{\frac{6}{u_b^2} \int_0^1 (1-\eta)\left(-\overline{\tilde{u}\tilde{v}}\right) \mathrm{d}\eta}_{C_{f,LT}} + \underbrace{\frac{6}{u_b^2} \int_0^1 (1-\eta)\left(-\overline{u''v''}\right) \mathrm{d}\eta}_{C_{f,ST}},
\end{aligned}
\tag{3.13}
$$

where $\eta = y/H$, $C_{f,L}$ denotes the laminar contribution, and $C_{f,LT}$ and $C_{f,ST}$ are the large-scale and small-scale turbulent contributions, respectively. Figure 19(*a*) shows that C_f increases monotonically with Ra and exceeds the isothermal open-Poiseuille reference value (dashed line). The decomposition indicates that, in the roll-containing regime ($10^6 \leq Ra \leq 10^7$), $C_{f,LT}$ varies only moderately, whereas it increases more strongly at $Ra = 10^8$, concomitant with the increasingly fragmented large-scale organisation (see figure 19*b*). In contrast, $C_{f,ST}$ grows rapidly with Ra (see figure 19*c*), mirroring the behaviour of the small-scale heat-transfer contribution Nu_S. The relative contributions in figure 19(*d*) reveal a crossover. For $Ra \leq 3 \times 10^6$, the large-scale component accounts for the larger fraction of C_f, whereas for $Ra \geq 10^7$ the small-scale component dominates. The transition occurs over $3 \times 10^6 < Ra < 10^7$, consistent with the corresponding crossover between Nu_L and Nu_S. A notable difference from Nu is that the large- and small-scale contributions to C_f become comparable again at $Ra = 10^8$. This behaviour contrasts with neutrally stratified open-channel turbulence at higher Reynolds numbers (Yao *et al.* 2022), where the small-scale contribution remains dominant, suggesting that the large-scale organisation in open PRB is dynamically distinct from the very-large-scale motions of isothermal open-channel flows.

3.3. *Velocity-dip model*

To describe the velocity-dip phenomenon observed in open PRB flows, we develop a model for the mean streamwise-velocity profile. Following previous analyses of closed PRB systems (Scagliarini *et al.* 2015) and canonical Poiseuille flow (L'vov *et al.* 2004), we assume that the mean turbulent kinetic energy (TKE) budget in the bulk region is approximately in equilibrium, with production balancing dissipation,

$$
P_B + P_S \approx \varepsilon_u, \tag{3.14}
$$

where P_B and P_S denote buoyancy and shear production, respectively, and ε_u is the TKE dissipation rate.

We first estimate $P_B = g\beta\,\overline{v'T'}$ from DNS-guided scalings. Figure 20(*a*) shows that P_B is approximately height-independent in the bulk region for $Ra \geq 10^6$. To rationalise this behaviour, we relate $\overline{v'T'}$ to the wall-normal transport of mean heat. This motivates the introduction of the local Nusselt number

$$
Nu_{\mathrm{local}}(y^*) = \sqrt{\frac{RaPr}{Ri_b}}\;\overline{v'^*T'^*}(y^*) - \frac{\partial \overline{T^*}}{\partial y^*}(y^*), \tag{3.15}
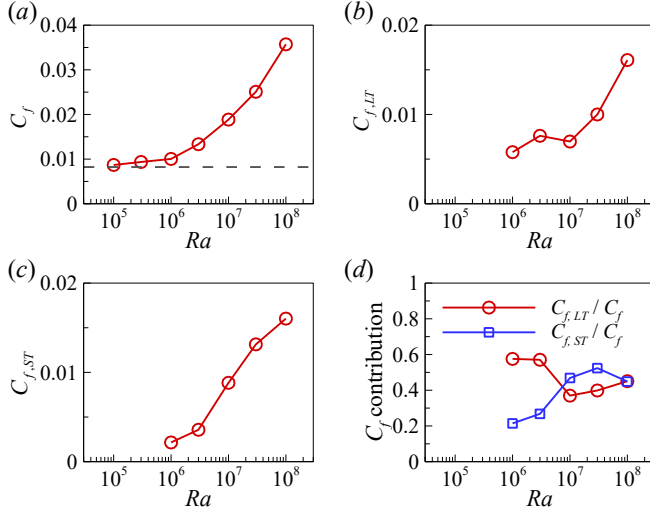$$

Figure 19. Friction coefficient as a function of the Rayleigh number Ra in the open PRB system. (*a*) Total friction coefficient C_f, (*b*) large-scale contribution $C_{f,LT}$, (*c*) small-scale contribution $C_{f,ST}$, and (*d*) relative contributions of the large- and small-scale components to C_f. The grey dashed line in (*a*) denotes the friction coefficient for open Poiseuille flow with temperature treated as a passive scalar at $Ra = 0$ and $Re_b = 2850$.

whose convective component $\sqrt{RaPr/Ri_b}\,\overline{v'^*T'^*}$ is proportional to P_B. Figure 21 further shows that $Nu_{\text{local}}(y^*)$ is nearly constant across the bulk. Moreover, for $Ra \geq 10^6$, enhanced mixing by the large-scale organisation renders the mean temperature gradient weak in the core, so that the conductive contribution $-\partial_{y^*}\overline{T^*}$ is negligible there. Therefore, the convective heat flux is approximately uniform in the bulk, implying an approximately height-independent buoyancy production, consistent with figure 20(*a*).

$$P_B = g\beta\,\overline{v'T'} = g\beta\,u_b\Delta_T\,\overline{v'^*T'^*} \approx \frac{Nu}{\sqrt{RaPr/Ri_b}}\,u_b g\beta\Delta_T \equiv C_1. \qquad (3.16)$$
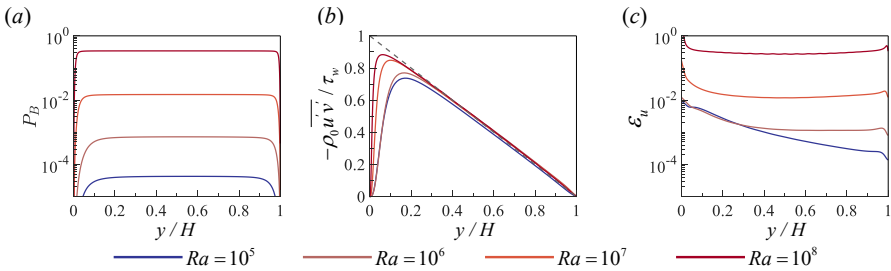

Figure 20. Wall-normal profiles of (*a*) buoyancy production P_B, (*b*) Reynolds shear stress $-\rho_0\overline{u'v'}$, and (*c*) dissipation rate ε_u for different Rayleigh numbers Ra at $Re_b = 2850$ and $Pr = 0.71$. The buoyancy production and dissipation rate in (*a*) and (*c*) are normalised by u_b^3/H. The dashed line in (*b*) represents a linear approximation for the shear stress to guide the eye.
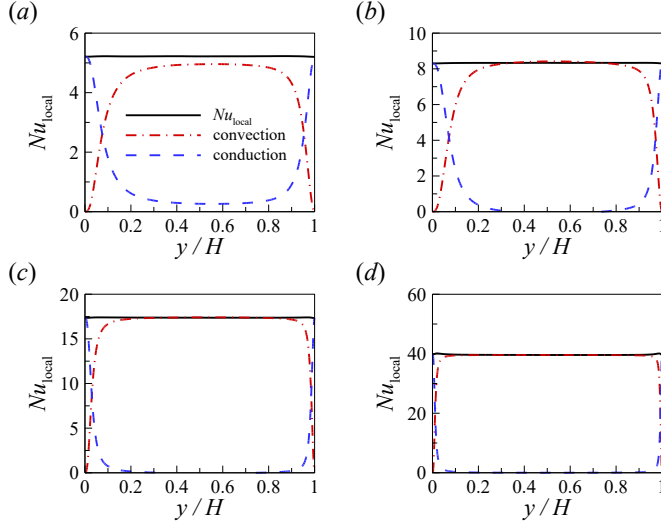
Figure 21. Wall-normal profiles of the local Nusselt number $Nu_{\text{local}} = \sqrt{RaPr/Ri_b}\,\overline{v'^*T'^*} - \partial_{y^*}\overline{T^*}$ and its convective $\sqrt{RaPr/Ri_b}\,\overline{v'^*T'^*}$ and conductive $-\partial_{y^*}\overline{T^*}$ contributions. Panels *(a–d)* correspond to $Ra = 10^5$, 10^6, 10^7, and 10^8 at $Re_b = 2850$ and $Pr = 0.71$.

We next model the shear production term $P_S = -\overline{u'v'}\,\mathrm{d}\overline{u}/\mathrm{d}y$. Guided by the DNS results (see figure 20*b*), we assume that $-\overline{u'v'}$ varies approximately linearly with y/H within the region where the velocity dip is observed,

$$-\overline{u'v'} \approx u_\tau^2\,(a' - b'\,y/H)\,. \tag{3.17}$$

The corresponding local shear-velocity scale is $u_{\tau,\text{loc}} = u_\tau\,(a' - b'\,y/H)^{1/2}$, and the shear production can be estimated as

$$P_S = -\overline{u'v'}\frac{\mathrm{d}\overline{u}}{\mathrm{d}y} \approx u_\tau^2\,(a' - b'\,y/H)\frac{\mathrm{d}\overline{u}}{\mathrm{d}y}. \tag{3.18}$$

Finally, we model the dissipation rate ε_u. Its wall-normal distribution evolves with Ra, from a shear-dominated profile that decreases monotonically with y to one that exhibits an approximately height-independent interior plateau once large-scale rolls develop (see figure 20*c*). Motivated by this behaviour, we decompose the dissipation into shear-induced and buoyancy-induced contributions,

$$\varepsilon_u = \nu\,\overline{\frac{\partial u'_i}{\partial x_j}\frac{\partial u'_i}{\partial x_j}} = \varepsilon_{u,S} + \varepsilon_{u,B}. \tag{3.19}$$

The shear-induced dissipation $\varepsilon_{u,S}$ is estimated using a local cascade argument, in which the dissipation balances the flux of TKE (Scagliarini *et al.* 2015; L'vov *et al.* 2004). Taking the TKE to be of the order of $-\overline{u'v'}$ and estimating the cascade time scale as $t_c \sim \ell_m/u_{\tau,\text{loc}}$, with mixing length $\ell_m = \kappa y$, yields

$$\varepsilon_{u,S} \approx \frac{\text{TKE}}{t_c} \approx \frac{k_1' u_\tau^2 \, (a' - b' \, y/H)}{\kappa y / \left[u_\tau \, (a' - b' \, y/H)^{1/2} \right]} = \frac{k_1 u_\tau^3 \, (a' - b' \, y/H)^{3/2}}{y}, \qquad (3.20)$$

where k_1 and k_1' are phenomenological parameters with $k_1 = k_1'/\kappa$. For the buoyancy-induced contribution $\varepsilon_{u,B}$, we interpret it as arising from mixing driven by large-scale structures and estimate it using the free-fall velocity u_f and the channel height H as characteristic scales,

$$\varepsilon_{u,B} \approx k_2 \frac{u_f^3}{H}, \qquad (3.21)$$

where k_2 is a phenomenological parameter.

Substituting (3.16)–(3.21) into (3.14) yields

$$C_1 + u_\tau^2 \, (a' - b' \, y/H) \, \frac{\partial \overline{u}}{\partial y} = \frac{k_1 u_\tau^3 \, (a' - b' \, y/H)^{3/2}}{y} + \frac{k_2 u_f^3}{H}, \qquad (3.22)$$

which can be rearranged as

$$\frac{\partial \overline{u}}{\partial y} = \frac{k_1 u_\tau \, (a' - b' \, y/H)^{1/2}}{y} + \frac{k_2 u_f^3/H - C_1}{u_\tau^2 \, (a' - b' \, y/H)}. \qquad (3.23)$$

In the bulk region, the Reynolds shear stress is approximately equal to the total shear stress (see figure 20b), so that $a' \approx b' \approx 1$. This leads to the simplified dimensionless form

$$\frac{\partial \overline{u}^+}{\partial y^*} \approx \frac{k_1 (1 - y^*)^{1/2}}{y^*} + \frac{(k_2 u_f^3/H - C_1)H}{u_\tau^3 (1 - y^*)}, \qquad (3.24)$$

where $y^* = y/H$ and $\overline{u}^+ = \overline{u}/u_\tau$. Integrating (3.24) gives

$$\overline{u}^+ \approx k_1 \left(2\sqrt{1 - y^*} - \ln\left(\frac{1 + \sqrt{1 - y^*}}{1 - \sqrt{1 - y^*}} \right) \right) - \frac{(k_2 u_f^3/H - C_1)H}{u_\tau^3} \ln(1 - y^*) + k_3, \quad (3.25)$$

where k_3 is an integration constant.

In the above model, three parameters, k_1, k_2 and k_3, remain to be specified, and we determine them by fitting the mean velocity profile. The constant k_1 and k_2 are inferred from the dissipation balance and subsequently validated against the DNS, while k_3 is constrained by a scaling argument. Specifically, k_1 controls the shear-induced dissipation through (3.20), k_2 controls the buoyancy-induced dissipation associated with large-scale structures (see (3.21)), and k_3 sets the additive level of $\overline{u}^+$, reflecting the magnitude of the mean velocity normalised by u_τ. The absence of simple closed-form expressions for $k_1(Ra)$ and $k_2(Ra)$ reflects the non-trivial coupling between shear and buoyancy, rather than a deficiency of the model. Nevertheless, their dependence on Ra is regular. Figures 22(a–c) show that the fitted parameters exhibit asymptotically consistent behaviour and follow approximately linear trends for $Ra \geq 10^7$. In particular, k_1 decreases as Ra increases (see figure 22a), consistent with a diminishing role of shear at higher buoyancy. The parameter k_2 varies non-monotonically, with a turning point around $Ra = O(10^7)$ (see figure 22b), which coincides with the regime transition from coherent streamwise rolls to convection cells. For k_3, we obtain the empirical fit $k_3 = 132.80 \, Ra^{-0.15}$ (see figure 22c). This scaling

is consistent with k_3 representing the order of $\overline{u}^+$, implying $k_3 \sim u_\tau^{-1} \sim Re_\tau^{-1}$. Indeed, the DNS yields $Re_\tau \sim Ra^{0.14}$ for $Ra \geq 10^6$ (see figure 22d), which is compatible with the observed $k_3(Ra)$. Using the values of k_1 and k_2 obtained at each Ra, we reconstruct the dissipation profiles via (3.20) and (3.21). Figure 22(e) shows that these reconstructed profiles agree closely with the DNS results, indicating that these parameters are not merely fitting constants for the velocity profile but also provide a consistent representation of the TKE dissipation.
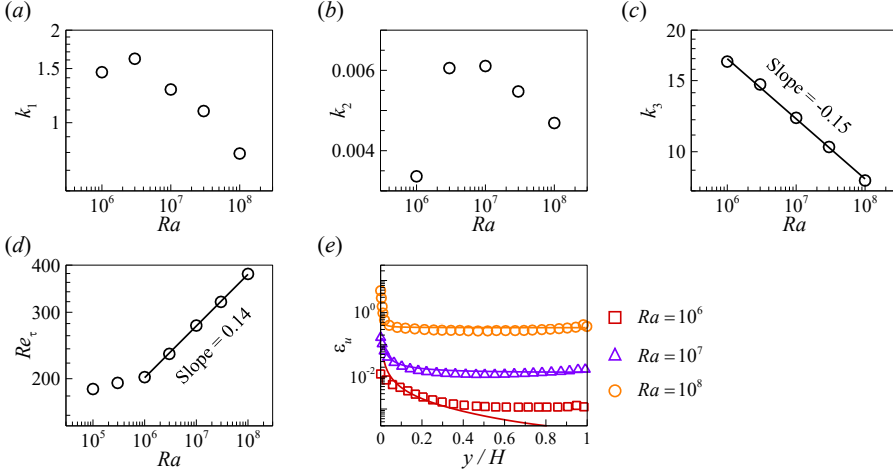

Figure 22. (*a–c*) Model parameters in equation (3.25) as functions of the Rayleigh number Ra. (*d*) Friction Reynolds number Re_τ as a function of Ra. (*e*) Wall-normal profiles of the dissipation rate ε_u, comparing DNS results (symbols) with model predictions obtained from equations (3.20)–(3.21) (solid lines).

Figure 23 compares the mean streamwise-velocity profiles and their wall-normal gradients predicted by equations (3.24)–(3.25) with DNS results at various Rayleigh numbers. Within the fitting range $y/H \in [0.2, 0.8]$, the relative error in the predicted mean velocity remains below 0.5% of the local value, indicating excellent agreement. As is evident from equations (3.24) and (3.25), discrepancies arise near the walls and near the free surface, where the linear approximation for the Reynolds shear stress breaks down and the buoyancy production is no longer height-independent owing to the dominance of thermal boundary layers. We also compare the present model with that of Scagliarini *et al.* (2015) in figure 23. While our model successfully reproduces the velocity-dip phenomenon, the model of Scagliarini *et al.* (2015) does not. A key limitation of that model is the assumption that the streamwise velocity gradient remains strictly positive, which enforces a monotonic velocity profile and therefore precludes the formation of a dip near the free surface. By contrast, the present model adopts a linear wall-normal distribution of the Reynolds shear stress rather than a constant order-of-magnitude estimate, incorporates a height-independent buoyancy-production term consistent with the DNS in the bulk region, and explicitly decomposes the dissipation into shear-induced and buoyancy-induced components. These elements allow a more faithful representation of the bulk dynamics in open PRB flows and enable the model to capture the observed velocity-dip behaviour.

To further clarify the relation between the present velocity-dip model and ABL theory, we compare our results with predictions from Monin–Obukhov similarity theory (MOST; Monin & Obukhov (1954)) for the mean streamwise-velocity profile. Since MOST is formally restricted to the surface layer, we include it here as a reference by extrapolating
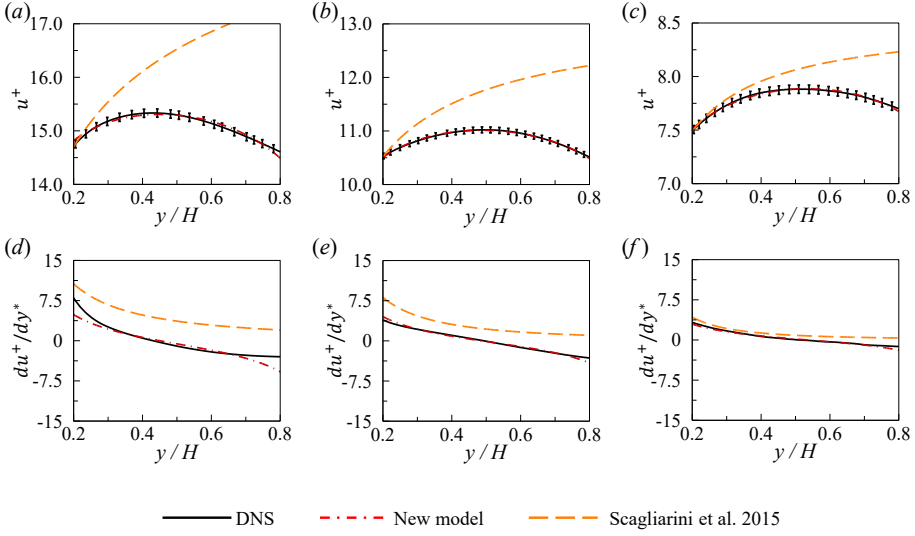
Figure 23. (*a–c*) Mean streamwise velocity and (*d–f*) wall-normal velocity gradient, normalised by the friction velocity u_τ and the open-channel height H. Comparison between the present model [equations (3.24) and (3.25)], the model of Scagliarini *et al.* (2015), and DNS results at (*a,d*) $Ra = 10^6$, (*b,e*) $Ra = 10^7$ and (*c,f*) $Ra = 10^8$ with $Re_b = 2850$. The shaded error bars in (*a–c*) indicate a relative model deviation within 0.5% of the local value.

the stability function across the fitting range $y/H \in [0.2, 0.8]$, in order to highlight qualitative differences with the DNS and the present model. In MOST, the mean velocity gradient is expressed as

$$\frac{d\overline{u}}{dy} = \frac{u_\tau}{\kappa y} \phi_m\left(\frac{y}{L_{MO}}\right), \qquad (3.26)$$

where ϕ_m is the stability function and L_{MO} is the Monin–Obukhov length. Among the available empirical formulations, we adopt the form recommended by Wilson (2001), which was calibrated against the extensive field dataset of Högström (1988). This formulation employs the standard von Kármán constant $\kappa = 0.40$ and exhibits the correct asymptotic behaviour in the strongly convective limit,

$$\phi_m\left(\frac{y}{L_{MO}}\right) = \left(1 + \gamma_m |y/L_{MO}|^{2/3}\right)^{-1/2}, \qquad \gamma_m = 3.6. \qquad (3.27)$$

Integrating the gradient yields the corresponding velocity profile,

$$\overline{u}^+ = \frac{1}{\kappa}\left[\ln(|y/L_{MO}|) - 3\ln\left(1 + \sqrt{1 + \gamma_m |y/L_{MO}|^{2/3}}\right)\right] + u_0^+, \qquad (3.28)$$

where the additive constant u_0^+ is chosen such that $\overline{u}^+$ matches the DNS value at $y/H = 0.2$, corresponding to the lower bound of the fitting range used in the velocity-dip model. Figure 24 compares the DNS results, the present velocity-dip model, and MOST predictions for $Ra = 10^6$, 10^7 and 10^8. MOST captures the overall logarithmic trend and its dependence on stability, but it does not reproduce the velocity-dip behaviour. This limitation arises because the stability function ϕ_m remains strictly positive under unstable stratification,
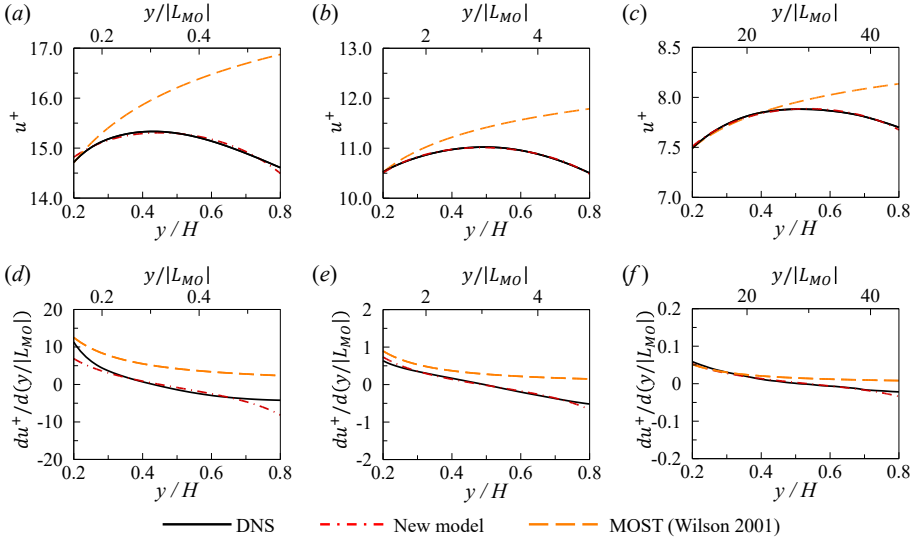
Figure 24. (*a–c*) Mean streamwise velocity and (*d–f*) wall-normal velocity gradient, normalised by the friction velocity u_τ and the Monin–Obukhov length L_{MO}. Comparison between the present model [equations (3.24) and (3.25)] and Monin–Obukhov similarity theory (MOST) using the stability function of Wilson (2001) [equations (3.27) and (3.28)], against DNS results at *(a,d)* $Ra = 10^6$, *(b,e)* $Ra = 10^7$ and *(c,f)* $Ra = 10^8$ with $Re_b = 2850$.

enforcing a monotonic mean velocity profile. By contrast, the present model permits a local reversal of the velocity gradient and the emergence of a velocity dip.

4. Conclusion

In this work, we have performed direct numerical simulations of turbulent mixed convection in an open PRB system, i.e. a PRB configuration with a free-slip upper boundary, to elucidate how buoyancy modulates the velocity distribution and heat transfer in open-channel flows. Our analysis identifies distinct flow regimes arising from the interplay between shear and buoyancy. At a fixed bulk Reynolds number $Re_b = 2850$, the flow is shear-dominated at low Rayleigh number ($Ra = 10^5$, corresponding to a bulk Richardson number $Ri_b = 0.017$). In this regime, the flow structures closely resemble those of canonical open Poiseuille flow, with buoyancy playing a negligible role. As the Rayleigh number increases to $10^6 \leq Ra \leq 10^7$ ($0.17 \leq Ri_b \leq 1.7$), shear and buoyancy become comparable, leading to the emergence of large-scale, streamwise-oriented rolls that dominate the flow dynamics. At higher Rayleigh number ($Ra = 10^8$, $Ri_b = 17$), the system transitions to a buoyancy-dominated regime in which the streamwise rolls fragment and the flow evolves towards a convection-cell-dominated state. Two-point correlations and premultiplied energy spectra show that the characteristic streamwise and spanwise extents of the rolls are approximately $12H$ and $4H$, respectively, whereas the convection cells are shorter than the rolls in both directions.

We next analyse the mean flow statistics in the open PRB system and find that buoyancy exerts a pronounced influence on both the velocity and temperature distributions. For $Ra \geq 10^6$, a distinct velocity dip emerges, with the maximum mean streamwise velocity located below the free-slip upper boundary. At the same time, the bulk temperature profile becomes increasingly uniform, indicating enhanced vertical mixing driven by buoyancy-induced

motions. To elucidate the origin of the velocity dip, we examine the role of large-scale convective rolls in shaping the mean velocity distribution and heat transfer. Short-time-averaged flow fields show that these rolls induce persistent low-speed regions near the upper boundary. A triple decomposition of the streamwise momentum equation further reveals that the large-scale structures play a dominant role in redistributing streamwise momentum. In particular, the near-surface momentum balance exhibits a large-scale Reynolds shear stress that locally exceeds the total shear stress, implying a negative viscous contribution and hence a reversal of the mean velocity gradient, which manifests as the velocity dip.

Finally, we develop a model to describe the velocity-dip phenomenon in the open PRB system. Assuming an approximate balance between buoyancy and shear production and dissipation, and incorporating a linear wall-normal profile of the Reynolds shear stress, a height-independent buoyancy-production term, and a decomposition of the dissipation into shear- and buoyancy-induced contributions, we derive a mean velocity profile that captures the velocity dip over the range $10^6 \leq Ra \leq 10^8$. Our model predictions show excellent agreement with the DNS results, with relative errors below 0.5%. We emphasise that the model is intended as a mechanistic, reduced description of the mean velocity profile and the associated velocity dip within this parameter range, rather than as a universal closure applicable to arbitrary values of Re_b and Ra. Extending its applicability to broader parameter regimes will require additional DNS data and is left for future work.

Declaration of interests. The authors report no conflict of interest.

Author ORCIDs Ao Xu, https://orcid.org/0000-0003-0648-2701; Heng-Dong Xi, https://orcid.org/0000-0002-2999-2694.

Appendix A. Validation of Nek5000 against benchmark data

We validate our Nek5000 implementation by comparing the present DNS results with established benchmark datasets for turbulent mixed convection in an open PRB channel and canonical open Poiseuille flow. For the mixed-convection benchmark, we use the reference data of Pirozzoli *et al.* (2017). Figure 25 compares the mean temperature and streamwise-velocity profiles, together with the root-mean-square (r.m.s.) fluctuations of temperature and all three velocity components, over the lower half of the channel ($0 \leq y/h \leq 1$) at $Re_b \approx 3162$, $Ra = 10^7$ and $Pr = 1$. For the open Poiseuille-flow benchmark, we compare our results with the datasets of Pirozzoli (2023) and Yao *et al.* (2022). Figure 26 shows the mean streamwise-velocity profile and the r.m.s. fluctuations of the streamwise, wall-normal and spanwise velocity components across the full channel height at $Re_b = 2850$. In both cases, the Nek5000 results closely match the benchmark data, demonstrating that the present numerical implementation accurately reproduces both mixed-convection and isothermal open-channel turbulence. This agreement supports the reliability of the DNS statistics reported in the main text.

Appendix B. Flow organisation in canonical open Poiseuille flow with a passive scalar

Figures 27 and 28 present representative instantaneous flow structures for canonical open Poiseuille flow with a passive scalar at $Ra = 0$, $Pr = 0.71$ and $Re_b = 2850$. In this reference case, buoyancy is absent and the temperature acts as a passive scalar, i.e. it is advected and diffused by the turbulent flow without feedback onto the momentum field. The flow organisation is therefore governed primarily by shear. Figure 27 shows instantaneous volume renderings of the passive-scalar field and the streamwise velocity. The flow is dominated by elongated streamwise-aligned structures characteristic of shear-driven turbulence. The passive scalar exhibits similar elongated patterns, reflecting its advection by near-wall and outer-layer motions. In contrast to buoyancy-driven cases, no coherent domain-spanning organisation is observed; the instantaneous field remains dominated by irregular, shear-generated structures. Further insight is provided by the x–z plane snapshots in figure 28,
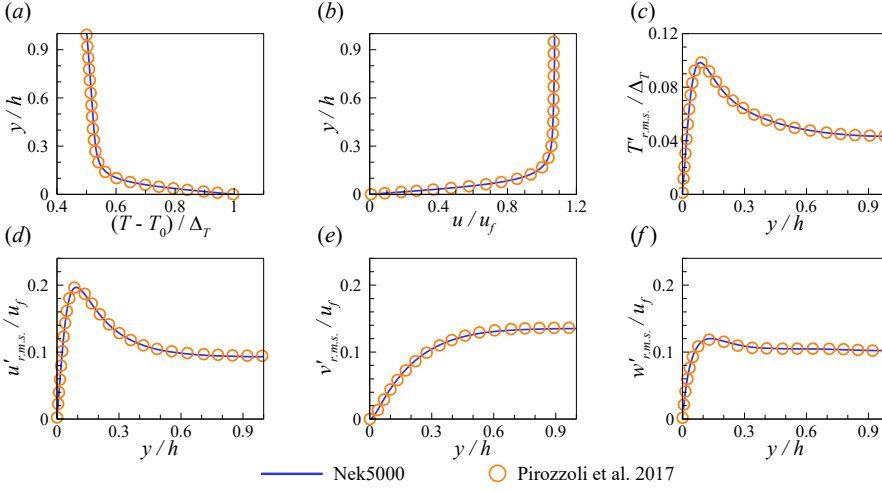
Figure 25. Comparison between the mixed-convection benchmark data of Pirozzoli *et al.* (2017) and the present Nek5000 results. Mean profiles of (*a*) temperature and (*b*) streamwise velocity, and root-mean-square (r.m.s.) fluctuations of (*c*) temperature, (*d*) streamwise velocity, (*e*) wall-normal velocity, and (*f*) spanwise velocity, evaluated over the lower half of the channel ($0 \leq y/h \leq 1$) at $Re_b \approx 3162$, $Ra = 10^7$, and $Pr = 1$.
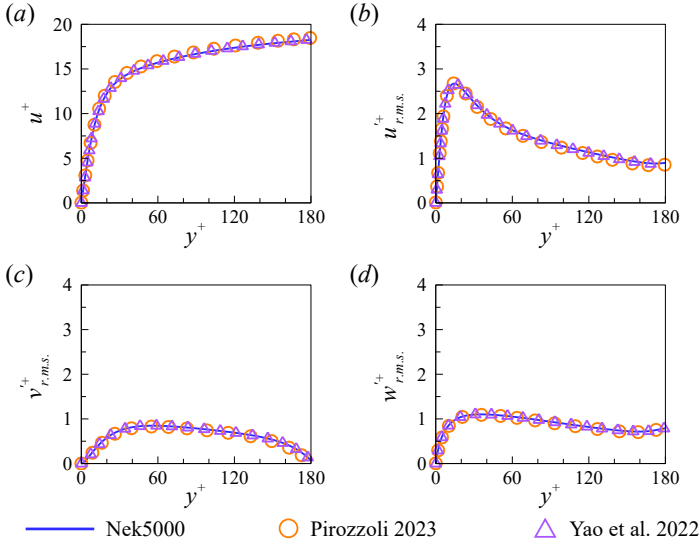

Figure 26. Comparison between the open Poiseuille-flow benchmark data of Pirozzoli (2023) and Yao *et al.* (2022) and the present Nek5000 results. Mean profiles of (*a*) streamwise velocity and root-mean-square (r.m.s.) fluctuations of (*b*) streamwise velocity, (*c*) wall-normal velocity, and (*d*) spanwise velocity, evaluated over the full channel height at $Re_b = 2850$.

which show contours of the streamwise velocity fluctuation u', the wall-normal velocity fluctuation v', and the scalar (temperature) fluctuation T' at three wall-normal locations: the near-wall region ($y^+ \approx 5$), the mid-plane ($y/H = 0.5$), and the near free-slip boundary ($y/H \approx 0.98$). Near the wall, the u' field displays the expected streaky organisation, while v' and T' appear in smaller, more fragmented patches consistent with ejection–sweep activity. Away from the wall, the structures become less streak-dominated and more spatially distributed. Near the free-slip boundary, the fluctuation fields remain dominated by relatively small-scale, intermittent features, without any indication of coherent roll-like organisation.
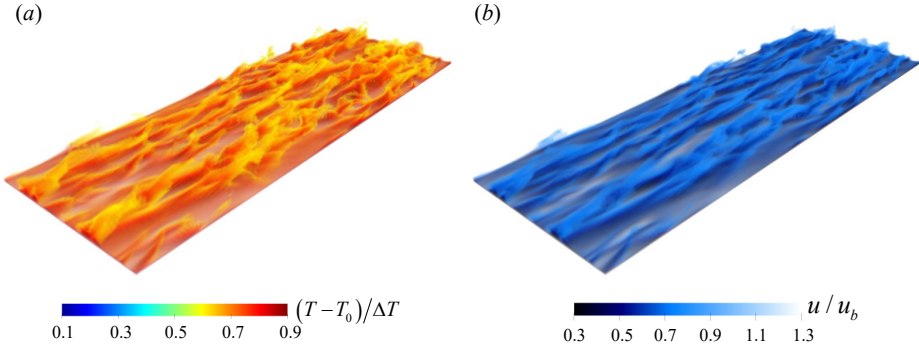
Figure 27. Instantaneous volume renderings of (*a*) temperature and (*b*) streamwise velocity for open Poiseuille flow with a passive scalar at $Ra = 0$, $Pr = 0.71$ and $Re_b = 2850$. The colour map and opacity transfer functions are identical to those used in figures 2 and 3.
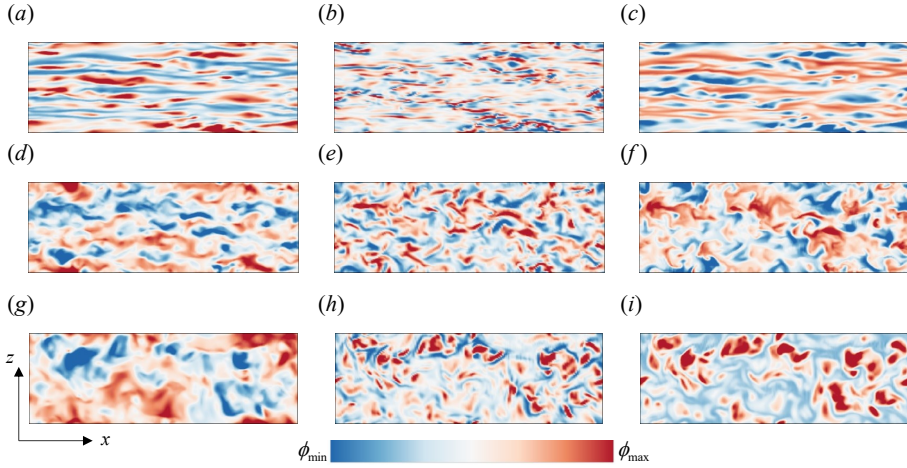

Figure 28. Typical instantaneous contours of *(a,d,g)* streamwise velocity fluctuation u', *(b,e,h)* wall-normal velocity fluctuation v' and *(c,f,i)* temperature fluctuation T' in the x–z plane for open Poiseuille flow with a passive scalar at $Re_b = 2850$. The contours are shown at three wall-normal locations: the near-wall region *(a–c, $y^+ \approx 5$)*, the mid-plane *(d–f, $y/H = 0.5$)*, and the near free-slip boundary *(g–i, $y/H \approx 0.98$)*. Contour levels correspond to ± 2 standard deviations of u', v' and T', respectively.

REFERENCES

AHAMED, N. & KUNDU, S. 2022 Application of the fractional entropy for one-dimensional velocity distribution with dip-phenomenon in open-channel turbulent flows. *Stoch. Environ. Res. Risk Assess.* **36** (5), 1289–1312.

ATOUFI, A., SCOTT, K.A. & WAITE, M.L. 2021 Kinetic energy cascade in stably stratified open-channel flows. *J. Fluid Mech.* **925**, A25.

BAUER, C., SAKAI, Y. & UHLMANN, M. 2023 Direct numerical simulation of turbulent open channel flow: streamwise turbulence intensity scaling and its relation to large-scale coherent motions. In *Conference on Interdisciplinary Turbulence Initiative*, pp. 311–317. Springer.

BERNARDINI, M., PIROZZOLI, S. & ORLANDI, P. 2014 Velocity statistics in turbulent channel flow up to $Re_\tau = 4000$. *J. Fluid Mech.* **742**, 171–191.

BLASS, A., TABAK, P., VERZICCO, R., STEVENS, R.J.A.M. & LOHSE, D. 2021 The effect of Prandtl number on turbulent sheared thermal convection. *J. Fluid Mech.* **910**, A37.

BLASS, A., ZHU, X.-J., VERZICCO, R., LOHSE, D. & STEVENS, R.J.A.M. 2020 Flow organization and heat transfer in turbulent wall sheared thermal convection. *J. Fluid Mech.* **897**, A22.

BROWN, E., NIKOLAENKO, A. & AHLERS, G. 2005 Reorientation of the large-scale circulation in turbulent Rayleigh-Bénard convection. *Phys. Rev. Lett.* **95** (8), 084503.

CASTILLO-CASTELLANOS, A., SERGENT, A., PODVIN, B. & ROSSI, M. 2019 Cessation and reversals of large-scale structures in square Rayleigh–Bénard cells. *J. Fluid Mech.* **877**, 922–954.

CAULFIELD, C.P. 2021 Layering, instabilities, and mixing in turbulent stratified flows. *Annu. Rev. Fluid Mech.* **53** (1), 113–145.

CHAUDHRY, M.H. 2022 *Open-channel flow*. Springer Nature Switzerland AG.

COSSU, C. 2022 Onset of large-scale convection in wall-bounded turbulent shear flows. *J. Fluid Mech.* **945**, A33.

COSSU, C., PUJALS, G. & DEPARDON, S. 2009 Optimal transient growth and very large–scale structures in turbulent boundary layers. *J. Fluid Mech.* **619**, 79–94.

CUI, Y., TAN, X., ZHANG, H. & ZHENG, X. 2025 Electrically driven relaminarisation of particle-laden turbulent channel flow. *J. Fluid Mech.* **1025**, A53.

DJENIDI, L., TARDU, S.F. & ANTONIA, R.A. 2013 Relationship between temporal and spatial averages in grid turbulence. *J. Fluid Mech.* **730**, 593–606.

DOMARADZKI, J.A. & METCALFE, R.W. 1988 Direct numerical simulations of the effects of shear on turbulent Rayleigh-Bénard convection. *J. Fluid Mech.* **193**, 499–531.

FENG, S.-J., LIU, H.-Y., LIU, H.-K. & ZHENG, X.-J. 2024 Comparisons of temperature structures with turbulent structures in thermally stratified channel flows by direct numerical simulation. *Int. J. Heat Fluid Flow* **105**, 109253.

FLORES, O. & RILEY, J.J. 2011 Analysis of turbulence collapse in the stably stratified surface layer using direct numerical simulation. *Bound.-Layer Meteor.* **139**, 241–259.

FUKAGATA, K., IWAMOTO, K. & KASAGI, N. 2002 Contribution of Reynolds stress distribution to the skin friction in wall-bounded flows. *Phys. Fluids* **14** (11), L73–L76.

GALANTI, B. & TSINOBER, A. 2004 Is turbulence ergodic? *Phys. Lett. A* **330** (3-4), 173–180.

HAY, W.A. & PAPALEXANDRIS, M.V. 2019 Numerical simulations of turbulent thermal convection with a free-slip upper boundary. *Proc. R. Soc. A-Math. Phys. Eng. Sci.* **475** (2232), 20190601.

HAY, W.A. & PAPALEXANDRIS, M.V. 2020 Evaporation-driven turbulent convection in water pools. *J. Fluid Mech.* **904**, A14.

HÖGSTRÖM, U.L.F. 1988 Non-dimensional wind and temperature profiles in the atmospheric surface layer: A re-evaluation. *Bound.-Layer Meteor.* **42** (1), 55–78.

HUANG, H.-L., XU, W., WANG, Y., WANG, X.-P., HE, X.-Z. & TONG, P. 2022 Fluctuation-induced slip of thermal boundary layers at a stable liquid–liquid interface. *J. Fluid Mech.* **951**, A10.

KADER, B.A. & YAGLOM, A.M. 1990 Mean fields and fluctuation moments in unstably stratified turbulent boundary layers. *J. Fluid Mech.* **212**, 637–662.

KHANNA, S. & BRASSEUR, J.G. 1998 Three-dimensional buoyancy-and shear-induced local structure of the atmospheric boundary layer. *J. Atmos. Sci.* **55** (5), 710–743.

KOOIJ, G.L., BOTCHEV, M.A., FREDERIX, E.M., GEURTS, B.J., HORN, S., LOHSE, D., VAN DER POEL, E.P., SHISHKINA, O., STEVENS, R.J.A.M. & VERZICCO, R. 2018 Comparison of computational codes for direct numerical simulations of turbulent Rayleigh–Bénard convection. *Comput. Fluids* **166**, 1–8.

LEE, J. & LEE, C. 2015 Modification of particle-laden near-wall turbulence: Effect of stokes number. *Phys. Fluids* **27** (2), 023303.

LOHSE, D. & SHISHKINA, O. 2024 Ultimate Rayleigh-Bénard turbulence. *Rev. Mod. Phys.* **96** (3), 035001.

LUIZ, E.W. & FIEDLER, S. 2024 Global climatology of low-level-jets: Occurrence, characteristics, and meteorological drivers. *J. Geophys. Res.-Atmos.* **129** (9), e2023JD040262.

L'VOV, V.S., POMYALOV, A., PROCACCIA, I. & TIBERKEVICH, V. 2004 Drag reduction by polymers in wall bounded turbulence. *Phys. Rev. Lett.* **92** (24), 244503.

MADHUSUDANAN, A., ILLINGWORTH, S.J., MARUSIC, I. & CHUNG, D. 2022 Navier-Stokes–based linear model for unstably stratified turbulent channel flows. *Phys. Rev. Fluids* **7** (4), 044601.

MONIN, A. S. & OBUKHOV, A. M. 1954 Basic laws of turbulent mixing in the atmospheric boundary layer. *Trudy Inst. Teor. Geofiz. Akad. Nauk SSSR* **24**, 163–187.

NIEMELA, J.J., SKRBEK, L., SREENIVASAN, K.R. & DONNELLY, R.J. 2001 The wind in confined thermal convection. *J. Fluid Mech.* **449**, 169–178.

PATERA, A.T. 1984 A spectral element method for fluid dynamics: laminar flow in a channel expansion. *J. Comput. Phys.* **54** (3), 468–488.

PINELLI, M., HERLINA, H., WISSINK, J.G. & UHLMANN, M. 2022 Direct numerical simulation of turbulent mass transfer at the surface of an open channel flow. *J. Fluid Mech.* **933**, A49.

PINO, D., VILÀ-GUERAU DE ARELLANO, J. & DUYNKERKE, P.G. 2003 The contribution of shear to the evolution of a convective boundary layer. *J. Atmos. Sci.* **60** (16), 1913–1926.

PIROZZOLI, S. 2023 Searching for the log law in open channel flow. *J. Fluid Mech.* **971**, A15.

PIROZZOLI, S., BERNARDINI, M. & ORLANDI, P. 2014 Turbulence statistics in Couette flow at high Reynolds number. *J. Fluid Mech.* **758**, 327–343.

PIROZZOLI, S., BERNARDINI, M. & ORLANDI, P. 2016 Passive scalars in turbulent channel flow at high Reynolds number. *J. Fluid Mech.* **788**, 614–639.

PIROZZOLI, S., BERNARDINI, M., VERZICCO, R. & ORLANDI, P. 2017 Mixed convection in turbulent channels with unstable stratification. *J. Fluid Mech.* **821**, 482–516.

REYNOLDS, W.C. & HUSSAIN, A.K.M.F. 1972 The mechanics of an organized wave in turbulent shear flow. Part 3. Theoretical models and comparisons with experiments. *J. Fluid Mech.* **54** (2), 263–288.

SALESKY, S.T. & ANDERSON, W. 2018 Buoyancy effects on large-scale motions in convective atmospheric boundary layers: implications for modulation of near-wall processes. *J. Fluid Mech.* **856**, 135–168.

SALESKY, S.T., CHAMECKI, M. & BOU-ZEID, E. 2017 On the nature of the transition between roll and cellular organization in the convective boundary layer. *Bound.-Layer Meteor.* **163** (1), 41–68.

SAULO, C., RUIZ, J. & SKABAR, Y.G. 2007 Synergism between the low-level jet and organized convection at its exit region. *Mon. Weather Rev.* **135** (4), 1310–1326.

SCAGLIARINI, A., EINARSSON, H., GYLFASON, Á. & TOSCHI, F. 2015 Law of the wall in an unstably stratified turbulent channel flow. *J. Fluid Mech.* **781**, R5.

SCAGLIARINI, A., GYLFASON, Á. & TOSCHI, F. 2014 Heat-flux scaling in turbulent Rayleigh-Bénard convection with an imposed longitudinal wind. *Phys. Rev. E* **89** (4), 043012.

SCHÄFER, K., FROHNAPFEL, B. & MELLADO, J.P. 2022 The effect of spanwise heterogeneous surfaces on mixed convection in turbulent channels. *J. Fluid Mech.* **950**, A22.

SCHOPPA, W. & HUSSAIN, F. 2000 Coherent structure dynamics in near-wall turbulence. *Fluid Dyn. Res.* **26** (2), 119.

SHISHKINA, O. & LOHSE, D. 2024 Ultimate Regime of Rayleigh-Bénard Turbulence: Subregimes and Their Scaling Relations for the Nusselt vs Rayleigh and Prandtl numbers. *Phys. Rev. Lett.* **133** (14), 144001.

SHISHKINA, O., STEVENS, R.J.A.M., GROSSMANN, S. & LOHSE, D. 2010 Boundary layer structure in turbulent thermal convection and its consequences for the required numerical resolution. *New J. Phys.* **12** (7), 075022.

SILANO, G., SREENIVASAN, K.R. & VERZICCO, R. 2010 Numerical simulations of Rayleigh–Bénard convection for Prandtl numbers between 10^{-1} and 10^4 and Rayleigh numbers between 10^5 and 10^9. *J. Fluid Mech.* **662**, 409–446.

SOUCASSE, L., PODVIN, B., RIVIÈRE, P. & SOUFIANI, A. 2019 Proper orthogonal decomposition analysis and modelling of large-scale flow reorientations in a cubic Rayleigh–Bénard cell. *J. Fluid Mech.* **881**, 23–50.

STENSRUD, D.J. 1996 Importance of Low-Level Jets to Climate: A Review. *J. Clim.* **9**, 1698–1711.

STEVENS, R.J.A.M., HARTMANN, R., VERZICCO, R. & LOHSE, D. 2024 How wide must Rayleigh–Bénard cells be to prevent finite aspect ratio effects in turbulent flow? *J. Fluid Mech.* **1000**, A58.

STEVENS, R.J.A.M., VAN DER POEL, E.P., GROSSMANN, S. & LOHSE, D. 2013 The unifying theory of scaling in thermal convection: the updated prefactors. *J. Fluid Mech.* **730**, 295–308.

STOLL, R., GIBBS, J.A., SALESKY, S.T., ANDERSON, W. & CALAF, M. 2020 Large-eddy simulation of the atmospheric boundary layer. *Bound.-Layer Meteor.* **177** (2), 541–581.

STULL, R.B. 2012 *An introduction to boundary layer meteorology*, , vol. 13. Springer Science & Business Media.

TOH, S. & ITANO, T. 2005 Interaction between a large-scale structure and near-wall structures in channel flow. *J. Fluid Mech.* **524**, 249–262.

VERMA, M.K. 2018 *Physics of buoyant flows: from instabilities to turbulence*. World Scientific.

WALKER, R., TEJADA-MARTÍNEZ, A.E., MARTINAT, G. & GROSCH, C. 2014 Large-eddy simulation of open channel flow with surface cooling. *Int. J. Heat Fluid Flow* **50**, 209–224.

WANG, B.F., ZHOU, Q. & SUN, C. 2020a Vibration-induced boundary-layer destabilization achieves massive heat-transport enhancement. *Sci. Adv.* **6** (21), eaaz8239.

WANG, Q., CHONG, K.-L., STEVENS, R.J.A.M., VERZICCO, R. & LOHSE, D. 2020b From zonal flow to convection rolls in Rayleigh–Bénard convection with free-slip plates. *J. Fluid Mech.* **905**, A21.

WECKWERTH, T.M., HORST, T.W. & WILSON, J.W. 1999 An observational study of the evolution of horizontal convective rolls. *Mon. Weather Rev.* **127** (9), 2160–2179.

WILSON, D.K. 2001 An alternative function for the wind and temperature gradients in unstable surface layers. *Bound.-Layer Meteor.* **99** (1), 151–158.

XI, H.-D. & XIA, K.-Q. 2008 Azimuthal motion, reorientation, cessation, and reversal of the large-scale circulation in turbulent thermal convection: a comparative study in aspect ratio one and one-half geometries. *Phys. Rev. E* **78** (3), 036326.

XIA, K.-Q. 2024 Unveiling the mystery of effective slip. *J. Fluid Mech.* **1000**, F5.

Xu, A., Li, R.-Q. & Xi, H.-D. 2025 Temporal modulation on mixed convection in turbulent channels. *J. Fluid Mech.* **1006**, A11.

Xu, A., Xu, B.-R. & Xi, H.-D. 2023 Wall-sheared thermal convection: heat transfer enhancement and turbulence relaminarization. *J. Fluid Mech.* **960**, A2.

Xu, A., Xu, B.-R. & Xi, H.-D. 2024 Particle transport and deposition in wall-sheared thermal turbulence. *J. Fluid Mech.* **999**, A15.

Yang, R., Ng, C.S., Chong, K.L., Verzicco, R. & Lohse, D. 2022 Do increased flow rates in displacement ventilation always lead to better results? *J. Fluid Mech.* **932**, A3.

Yang, S.-Q., Tan, S.-K. & Lim, S.-Y. 2004 Velocity distribution and dip-phenomenon in smooth uniform open channel flows. *J. Hydraul. Eng.-ASCE* **130** (12), 1179–1186.

Yang, S.-Q., Xu, W.-L. & Yu, G.-L. 2006 Velocity distribution in a gradually accelerating free surface flow. *Adv. Water Resour.* **29** (12), 1969–1980.

Yao, J., Chen, X. & Hussain, F. 2022 Direct numerical simulation of turbulent open channel flows at moderately high Reynolds numbers. *J. Fluid Mech.* **953**, A19.

Yerragolam, G.S., Howland, C.J., Stevens, R.J.A.M., Verzicco, R., Shishkina, O. & Lohse, D. 2024 Scaling relations for heat and momentum transport in sheared Rayleigh–Bénard convection. *J. Fluid Mech.* **1000**, A74.

Zhang, H. 2024 Structure and coupling characteristics of multiple fields in dust storms. *Acta Mech. Sin.* **40** (3), 123339.

Zhou, Z.-S., Wang, Y.-X., Zhang, S.-H., Huang, W.-X. & Xu, C.-X. 2024 Influence of outer large-scale motions on near-wall structures in compressible turbulent channel flows. *J. Fluid Mech.* **994**, A14.

Zhou, Z.-S., Xu, C.-X. & Jiménez, J. 2022 Interaction between near-wall streaks and large-scale motions in turbulent channel flows. *J. Fluid Mech.* **940**, A23.